Advanced Functional Materials

ADVANCED FUNCTIONAL MATERIALS
www.afm-journal.de

RESEARCH ARTICLE OPEN ACCESS

Assembly of Cell-Seeded 3D Printed Hydrogel Modules with Perfusable Channel Networks

Zachary J. Geffert[1] | Daniel Fougnier[1] | Bo Van Durme[2] | Jenna Grutzmacher[1] | Ryan Clarke[1] | Susan Cao[1] | Zhenghao Li[1] | Ujjwal Aryal[1] | Jason A. Horton[3] | Sandra Van Vlierberghe[2] | Pranav Soman[1]

[1]Department of Biomedical and Chemical Engineering, Syracuse University, Syracuse, New York, United States | [2]Polymer Chemistry and Biomaterials Group, Department of Organic and Macromolecular Chemistry, Ghent University, Ghent, Belgium | [3]Department of Neuroscience and Physiology, SUNY Upstate Medical University, Syracuse, New York, United States

Correspondence: Pranav Soman (psoman@syr.edu)

Received: 8 February 2026 | **Revised:** 22 March 2026 | **Accepted:** 24 March 2026

Keywords: 3D printing | bioink | bioreactor | cell seeding | macroscale assembly | projection stereolithography

ABSTRACT

Successfully recapitulating functional tissue-scale biological structures using additive manufacturing requires simultaneous scaling up to reach clinically relevant sizes and scaling down to incorporate internal vascular-like features to support high cell viability. This work reports a new multiscale assembly method that integrates cell-seeded hydrogel modules via gluing to create larger constructs. Scalability is based on an intuitive concept of stacking modules, which allows for a high degree of geometric freedom without the need for specialized equipment. Projection Stereolithography (PSLA) is used to print centimeter-sized modules using gelatin methacryloyl aminoethyl methacrylate (GelMA-AEMA). Each module (500 mm^3) contains two independent hollow features: seeding port-arrays to facilitate cell seeding and branched channel networks to enable perfusion. New multi-material bioreactors are developed, integrating a rigid core with a flexible skin featuring needle septa to yield a watertight seal, providing a sterile environment for perfusion culture. In parallel, a novel gluing strategy is developed, and its efficacy is demonstrated by perfusing dye through an 18-module assembly. For cell-seeding experiments, model stromal cells are seeded within a 2-module assembly, followed by media perfusion. Through assembly of pre-printed perfusable hydrogel modules, this work helps address key limitations of existing methods and advances development toward realizing large-scale reproducible tissue constructs.

1 | Introduction

While remarkable progress has been made with small-sized tissue constructs, bioprinting large-scale, viable tissues continues to present significant challenges. Principal among these is the introduction of cells into the extracellular matrix (ECM) mimicking scaffolds and keeping them viable until their functional maturation. Traditional seeding of cells within clinically relevant-sized scaffolds often results in low, nonuniform cell density and poor nutrient diffusion [1, 2]. On the other hand, bioprinting methods rely on encapsulating cells within hydrogel-based ECM analogs, at the expense of exposing cells to increased mechanical or chemical stress during processing. This restricts the choice of compatible materials, and even impedes cell proliferation if the matrix is not optimized [1, 3]. Depending on the printing method, high-viscosity or photo-sensitive bioinks are often necessary, which expose cells to harsh conditions and reduce cell viability. Additionally, it is often difficult to achieve print fidelity

Zachary J. Geffert and Daniel Fougnier contributed equally to this work.

using cell-friendly bioinks. To ensure cell viability within large-scale constructs, an internal vascular-like perfusable network is required. However, printing such complex designs at scale is time-consuming, further reducing cell viability. Attempts to increase print speeds expose cells to damaging forces or require more intense curing steps (in light-based methods), which again can lower cell viability. Thus, despite many advances, the generation of viable human-scale tissues remains challenging due to the often contrasting relationships between print volumes, cell viability during and after printing, and design flexibility [4–9].

To overcome these constraints, macroscale assembly approaches have emerged, in which smaller high-fidelity prefabricated modules are combined to generate larger tissue constructs [10–13]. For instance, puzzle-inspired modular units and cryo-printed building blocks were used to construct organ-scale structures while preserving microscale organization [11, 14–16]. These methods, however, are often limited by the need for precise alignment during assembly, long fabrication times, and challenges in integrating perfusable networks throughout large constructs to maintain sufficient cell viability. Self-assembling cell-laden micro-niches offer high cellular density and microarchitecture control but face difficulties in maintaining structural stability and reproducibility across large tissue volumes [11]. Modular synthetic tissues and microbead-based assemblies demonstrate scalability and functional vascularization in centimeter-sized constructs [17–20]. Hydrogel localization platforms and modularized bioprinting strategies enhance spatial guidance and morphogenesis within assembled constructs [21, 22]. Still, they often require complex fabrication setups, specialized materials, and careful optimization of bioink properties to maintain fidelity. Other bottom-up tissue engineering strategies, including spheroid/organoid-based assembly and self-assembling cellular modules, provide modular fabrication of organized tissues [23–26]. Despite their versatility, these methods can be limited by challenges in scaling to clinically relevant sizes and difficulties in achieving functional perfusable networks throughout the assembled constructs. Recent reviews emphasize the promise of integrating these strategies while acknowledging remaining technical hurdles, such as module fusion, heterogeneity, and reproducibility [10, 12, 27].

By leveraging macroscale assembly of 3D printed and biofabricated modules, the field is moving closer to producing large, functional tissue constructs with precise internal architecture, bridging the gap between microscale resolution and clinically relevant tissue size. Nonetheless, each method still faces critical limitations in scalability, structural integration, and biological functionality, highlighting the need for continued innovation in modular, multiscale assembly techniques to achieve clinically viable tissues. This work reports a new macroscale assembly method in which individually printed dual-functionalized gelatin methacryloyl aminoethyl methacrylate (GelMA-AEMA) modules ($10 \times 10 \times 5$ mm^3) with embedded seeding port-arrays and branched channels can be assembled into large-scale perfusable constructs. Use of seeding port-arrays decouples scaffold manufacturing from cellularization, alleviating print time restrictions associated with encapsulation-based methods. Further reported is an open source, scalable multi-material perfusion bioreactor platform developed to facilitate gluing and perfusion of multi-module assemblies. Module positioning is guided by the bioreactor walls to aid in the alignment of perfusion channels, enhancing reproducibility. These key advancements have been used in conjunction to prepare both cellularized and acellular perfusable assemblies, measuring $20 \times 10 \times 5$ mm^3 (2-module) and $60 \times 30 \times 5$ mm^3 (18-module), respectively.

2 | Results

2.1 | New Macroscale Assembly Method

This new assembly approach is loosely inspired by plastic interlocking construction toys, in which individual modules fit together in various configurations to build a larger model. To highlight this inspiration, a typical liver model has been modularized to represent the individual modules that can be glued together and seeded to create this ideal large-scale construct. Figure 1 outlines the method of macroscale assembly of individually printed hydrogel modules from start to finish, beginning with the computer-aided design (CAD) model and ending with perfusion of glued constructs. To begin, hydrogel modules with branched, perfusable channels and seeding ports were modeled in CAD (Figure 1a) with outer dimensions of $10 \times 10 \times 5$ mm^3 (1 module). Branched channel geometry was optimized using the Hagen-Poiseuille equation (Supporting Information equation E1) for volumetric flow rate to ensure backpressure remained low along the flow path. For the purposes of this calculation, it is assumed that channels are circular and that media viscosity is equal to that of pure water. Perfusion channels halve in width at each branch, ranging from 1000 to 250 μm. 250 μm represents the smallest horizontal channel width that could be reliably printed and successfully cleared for perfusion. As such, this reflects the practical resolution limit of the existing printer hardware and resin formulation. Seeding port surface area was increased by incorporating Allihn condenser-inspired undulations. Additionally, the shallow sloping surfaces allowed cells to settle at regular intervals along the vertical channel. Previous iterations with straight channels yielded more cells settling to the bottom. Following CAD generation, the geometry was sliced into a series of photomasks (Figure 1b). Hydrogel structures were then prepared using a PSLA printer via sequential exposure of the photomasks at a layer height of 50 μm (Figure 1c). Following printing, hydrogel modules were incubated in phosphate-buffered saline (PBS) at 37°C with 100 rpm shaking for 24 h to wash away excess uncured resin (Figure 1d). The structures were subjected to an additional wash in fresh culture media under the same conditions for a further 24 h (Figure 1e). Washed hydrogels were loaded into assembled bioreactors, and resin was pipetted between the gel interface(s) (Figure 1f). After installing the lids and a fused deposition modeling (FDM) printed mask, the gels were glued together via photo-crosslinking in an LED curing chamber (B9A-LCB-010, B9 Creations, Rapid City, SD, USA) within an incubator at 37°C (Figure 1g). To prevent occlusion of channels with crosslinked resin, a syringe pump (NE-300 Single Channel, New Era, Farmingdale, NY, USA) was used to flow sterile air through the structures during crosslinking. Initial gluing trials were attempted using perfusion with liquid (PBS); however, due to wicking along the hydrogel surface, glue was diluted at the interface, and gels did not adhere. Successful gluing using air is attributed to both the large viscosity difference between water and air and their relative immiscibility. Glued

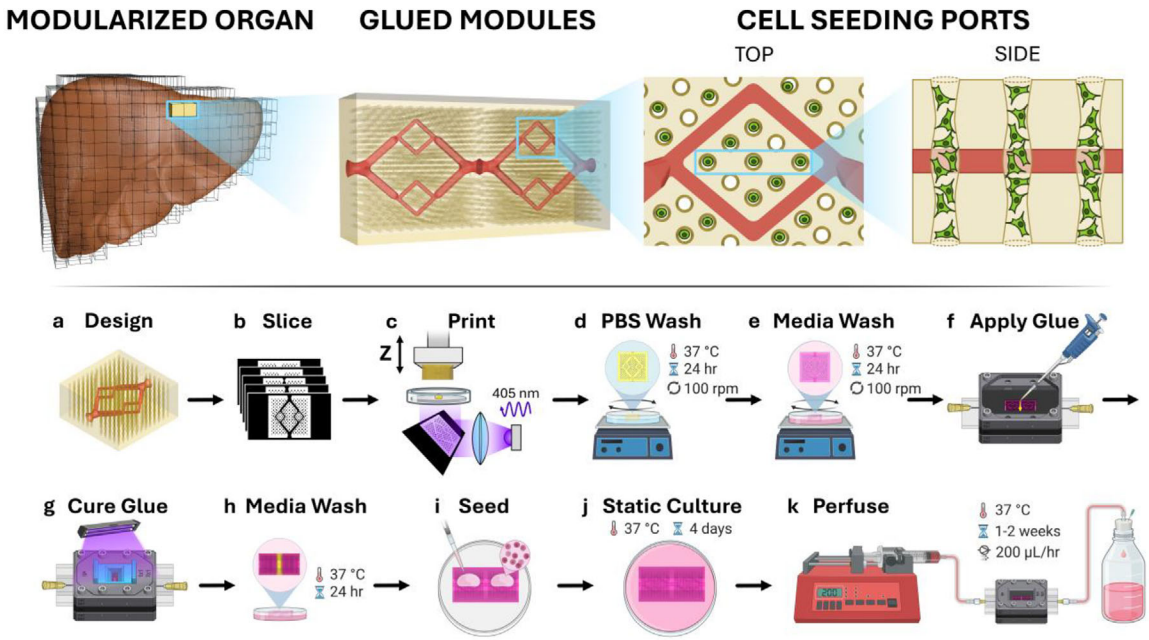

FIGURE 1 | New macroscale assembly method steps. (Top) Organ model is broken down into subunits, representing glued and seeded modules. (Bottom) (a) 3D CAD model of module structure with vascular-like branching internal architecture, including vertical seeding ports. (b) CAD model was sliced to generate masks for printing. (c) Slices were utilized to print a CAD model in 3D on a PSLA printer. Printed modules were washed in (d) PBS and (e) culture media for 24 h each at 37°C while shaking at 100 rpm. (f) Glue was applied to adhere multiple modules and (g) cured in a UV chamber. (h) A second wash in culture media followed gluing and preceded (i) cellular seeding from the top of glued constructs. (j) Constructs remained in static culture for 4 days and (k) were placed into a bioreactor and underwent perfusion for up to 2 weeks. Created in https://BioRender.com.

structures were removed from bioreactors and washed in culture media at 37°C for an additional 24 h (Figure 1h). Stromal cells were seeded on top of the constructs via a micropipette, with the cell suspension continuously returned to the top surface for 20 min. Constructs were then rotated 90 degrees and incubated for 30 min at 37°C (Figure 1i). Seeded constructs remained in static culture for 4 days preceding the beginning of perfusion (Figure 1j). After loading glued hydrogel constructs into bioreactors, needles were inserted through the needle septa and into the hydrogel inlet to a depth of approximately 1 mm. Next, the lids were installed, with all fasteners torqued to 0.15 N·m. Cell-laden structures were initially perfused with media at a rate of 50 µL min^{-1} to verify flow through the bioreactors and the absence of leaks (Figure 1k). Bioreactors were sealed and transported to an incubator at 37°C where flow was resumed at a reduced rate of 3.33 µL min^{-1} (200 µL h^{-1}). 200 µL h^{-1} was selected as it perfuses approximately five volume equivalents through the glued construct per day without exceeding 1 dyne cm^{-2} [28–30]. This target volume replacement was determined to support a desired concentration of 2 million cells mL^{-1}. Media was replenished in the syringe pump as needed.

2.2 | Material Selection

2.2.1 | Physico-Chemical Properties of GelMA-AEMA

Gelatin methacryloyl (GelMA) has been extensively utilized in biofabrication due to its excellent biocompatibility, biodegradability, and its ability to form photo-crosslinkable hydrogels that mimic the native ECM, providing a conducive environment for cell attachment, proliferation, and tissue regeneration (Figure S1a) [31–33]. However, the photo-crosslinkable functionalities in GelMA are inherently limited by the availability of primary amine groups in gelatin, which restricts the degree of methacrylation and consequently the density of the crosslinked network. To address this limitation, in 2017, Van Hoorick et al. introduced a gelatin derivative, GelMA-AEMA, which incorporates a higher amount of photoreactive functionalities, thereby enhancing the crosslinking potential and improving mechanical and processing properties relevant to light-based 3D printing [34]. Both GelMA and GelMA-AEMA were synthesized following the established reaction scheme (Figure S1a). Characterization by proton nuclear magnetic resonance spectroscopy (^{1}H NMR) revealed distinct proton peaks corresponding to methacrylamide (5.50 and 5.70 ppm) and AEMA moieties (5.80 and 6.20 ppm), with the degree of substitution quantified as 97 % for methacrylamide and a 22 % substitution for carboxyl groups relative to valine, leucine, and isoleucine reference peaks at 1 ppm in gelatin (Figure S1b,c).

Photorheological assessment of 15 wt/v% polymer solutions containing 2 mol% Li-TPO photoinitiator at 37°C demonstrated that GelMA-AEMA exhibited faster crosslinking kinetics, as evidenced by a notably lower required UV dose compared to GelMA (320 ± 3 mJ cm^{-2} vs. 615 ± 2 mJ cm^{-2}) (Figure 2a–c). This accelerated crosslinking in GelMA-AEMA is advantageous for light-based 3D printing, as it reduces processing time and enhances fabrication efficiency [35]. Prior studies report an approximately threefold increase in storage modulus (G′) for 15 wt/v% GelMA-AEMA hydrogels compared to GelMA at the same concentration at 37°C (147.1 ± 2.9 kPa vs. 47.5 ± 0.8 kPa) [34].

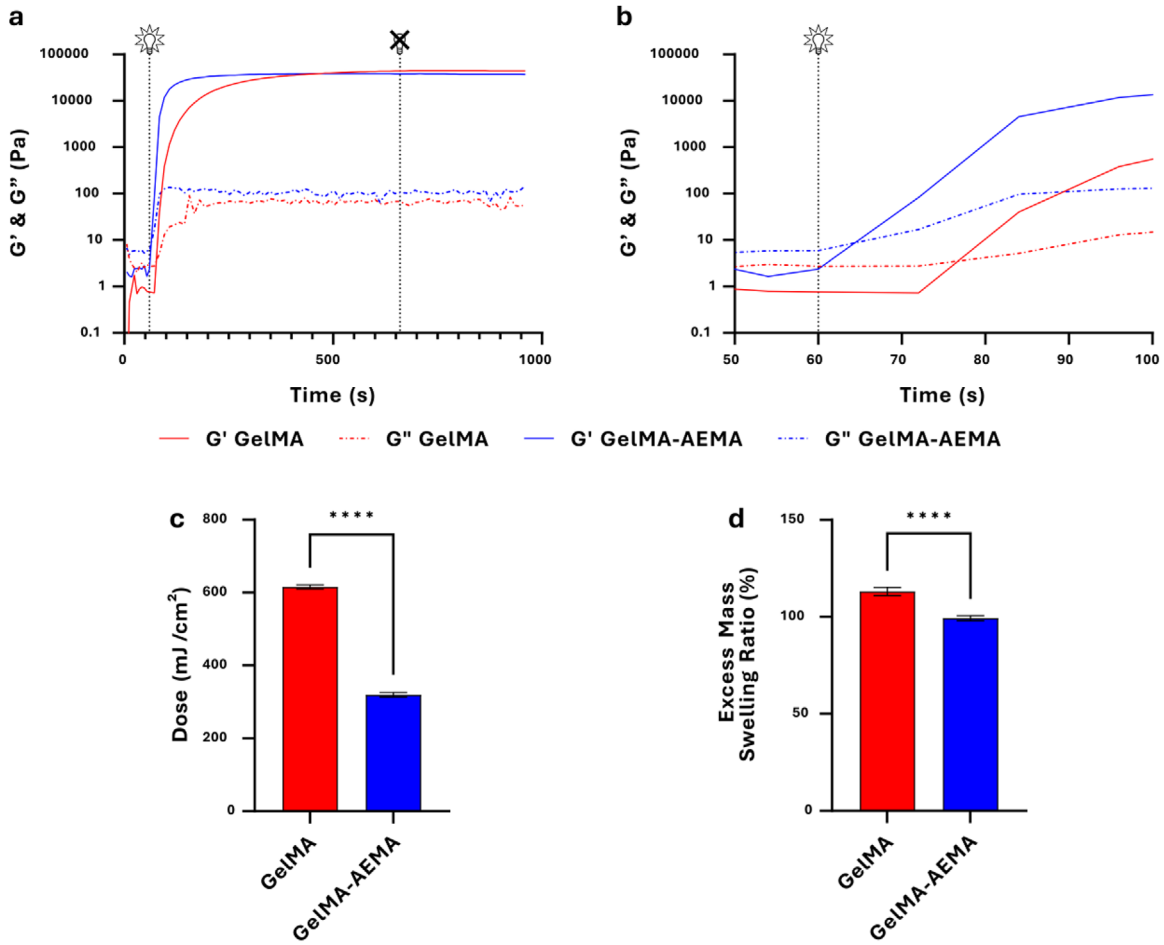

FIGURE 2 | Material selection. (a) Photorheological result for both GelMA and GelMA-AEMA. (b) Zoom in to region of interest between 50 and 100 s. (c) Dose comparison between the two materials. (****$p < 0.0001$, $n = 3$, Welch's t-test) (d) Excess mass swelling ratios for hydrogel samples prepared from GelMA and GelMA-AEMA, representing post-print swelling following incubation in PBS. An excess mass swelling ratio of 100 % indicates the absence of swelling. (****$p < 0.0001$, $n = 4$, Welch's t-test) Graphs were rendered in GraphPad Prism.

Another very important factor considered in material selection was post-print swelling. Excess swelling of hydrogel modules beyond their as-printed dimensions results in poor fitment within bioreactors, causing compression which can impair flow through open lumens. While the equilibrium swelling ratio is often reported as a metric for comparing hydrogel swelling in an absolute sense, it is not directly representative of excess swelling following incubation of printed hydrogels in isotonic media. Consequently, the excess mass swelling ratio, defined here as the ratio of swollen mass to as-printed mass, is reported to characterize post-print swelling in PBS. Note that the absence of swelling would result in an excess mass swelling value of 100 %. By this metric, samples prepared from GelMA exhibited a substantial degree of post-print swelling, with an excess swelling ratio of 113.0 ± 2.1 % (Figure 2d). In contrast, samples prepared from GelMA-AEMA exhibited virtually no additional swelling, with an excess swelling ratio of 99.3 ± 1.3 % (Figure 2d). This effect arises from the denser crosslinked network in GelMA-AEMA, which influences the mechanical properties of the hydrogel constructs [34, 35]. The absence of additional post-print swelling makes GelMA-AEMA exceptionally well-suited for use in conjunction with the perfusion bioreactors presented in this work.

2.2.2 | Cell Viability in GelMA-AEMA

Another important criterion for material selection, cell viability, was examined using mouse embryonic fibroblast cells (C3H10T1/2) within GelMA-AEMA to ensure high cellular resilience over the length of perfusion experiments. 5 mm diameter × 1.2 mm disks containing a 30 million cells mL^{-1} cell suspension in a 9:1 cell:hydrogel ratio were cast and crosslinked in a commercial UV curing chamber for 30 s. Following crosslinking, disks were placed in static culture for the duration of each timepoint. Figure S2 highlights cell viability through live dead staining with cells encapsulated within the material. By the 2-week endpoint, cell viability remained above 75 %. In accordance with ISO 10993-5, this produced a non-cytotoxic result with the threshold being 70 % [36]. The drop in viability on Day 3 can be understood as the cells adapting to their new encapsulated environment.

2.2.3 | Print Fidelity of GelMA-AEMA

Once high viability was confirmed, print fidelity was characterized to validate the ability to fabricate the desired CAD

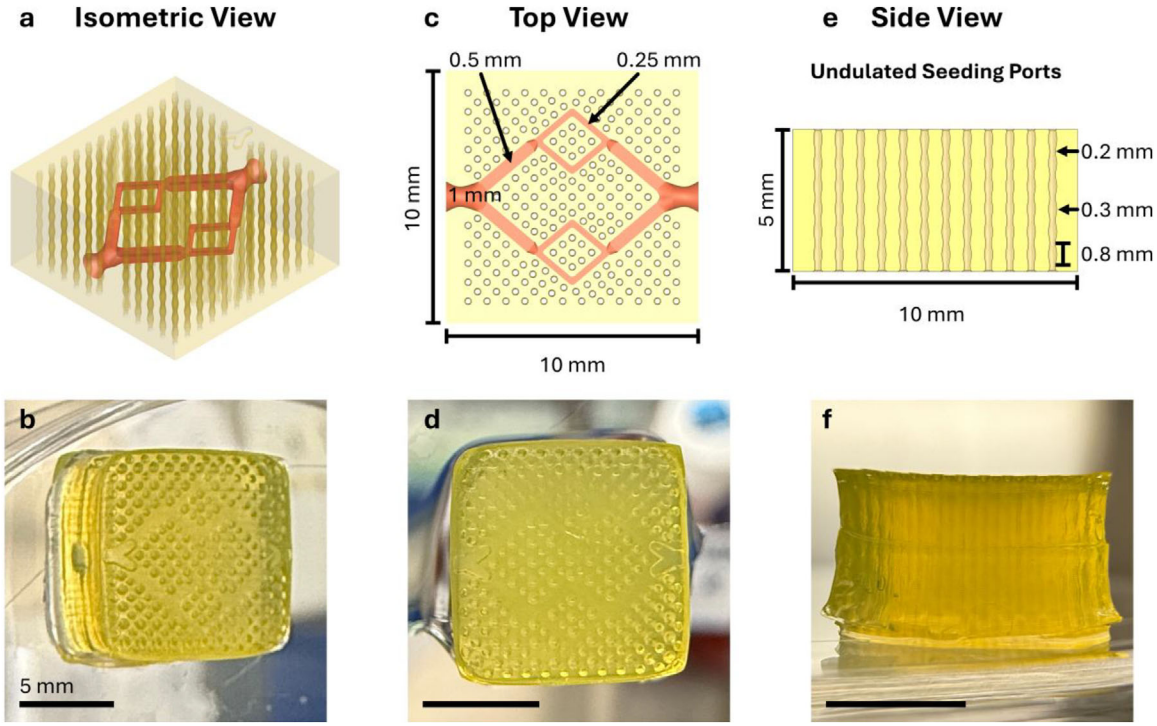

FIGURE 3 | Module design and printing. (a) Isometric CAD view and (b) respective printed result. (c) Top CAD view identifying internal geometry scales and (d) respective printed result. (e) Side CAD view highlighting undulated vertical seeding ports and (f) respective printed result. All scale bars are 5 mm.

model featuring vascular-like architecture with open lumens. To facilitate even temperature control and prevent physical gelation of the material within the vat, a silicone heater with an integrated thermocouple was incorporated into the vat holder design (Figures S3 and S4). The existing vat holder design was machined to allow the addition of a 1.75″ OD 10W silicone heater (MPI Morheat Inc., Toronto, ON, CA) with 1″ cutout in the center to facilitate light transmission without otherwise altering printer function. Two models were created, one to examine XY resolution (Figure S5a,b) and the other for Z resolution (Figure S6a,b). Both models include an array of lumens from 200 to 500 μm, with features visible from the top view and side view for XY and Z, respectively. Module geometry was perfused with 2 MDa FITC-Dextran to visualize channel patency (Figure S7). Open lumens were achieved in both XY and Z through the full range of tested diameters (Figure S5c–f; Figure S6c–f). Printing parameters used to achieve open lumens in test constructs were utilized to design and print final CAD models featuring more complex branched flow paths and undulating seeding ports. The isometric view highlights the branching, vascular-like architecture within the module, designed to supply nutrients to cells seeded in the seeding ports. These ports are arranged in a grid-like pattern throughout the construct (Figure 3a). The top view gives details on the specific dimensions, including an XY footprint of 10 mm × 10 mm where the branching architecture splits from 1 mm at the inlet to 500 μm and again down to 250 μm (Figure 3b). This pattern is mirrored toward the outlet. In the Z dimension, the module is 5 mm tall and features an array of undulated seeding ports patterned throughout, excluding regions that would intersect with the internal geometry (Figure 3c). The diameters of the undulated seeding ports oscillate from 200 to 300 μm with a wavelength of 800 μm (Figure 3c). Three views of printed results are shown below (Figure 3b,d,f). Z-bleed compensation was applied to the mesh geometry to increase the dimensional accuracy of negative features. Z-bleed occurs when the curing depth exceeds the intended layer height, causing unwanted polymerization in adjacent layers and resulting in dimensional inaccuracies and overcured lumens. Figure S8 highlights the effect of Z-bleed within this material and process.

2.3 | Design and Fabrication of Perfusion Bioreactors

To facilitate macroscale assembly using individual modules, new custom perfusion bioreactors were required to house the constructs. Scalable FDM 3D printed perfusion bioreactors were designed to accommodate arrays of hydrogels with 10 mm × 10 mm profiles, corresponding closely to the maximum build area of our PSLA printer. Similar approaches have been utilized to generate perfusion bioreactors which interface with individual hydrogel slabs. This existing design utilized a rigid FDM printed thermoplastic frame with gaskets and needle septa formed via casting of Sylgard 184 poly(dimethylsiloxane) (PDMS) into troughs modeled into the part [37]. While effective at a small scale, this manufacturing approach can prove difficult for the creation of larger bioreactors, as inconsistencies in the manual PDMS pour can result in inadequate sealing. Fabrication of bioreactors in this manner was a multi-day process, as PDMS must be poured twice to form gaskets on both the top and bottom sealing surfaces. To enhance reproducibility, manufacturing throughput, and scalability, multi-material FDM 3D printing was leveraged to eliminate the need for post-processing with PDMS. Bioreactors were designed as two bodies printed in different materials: a rigid

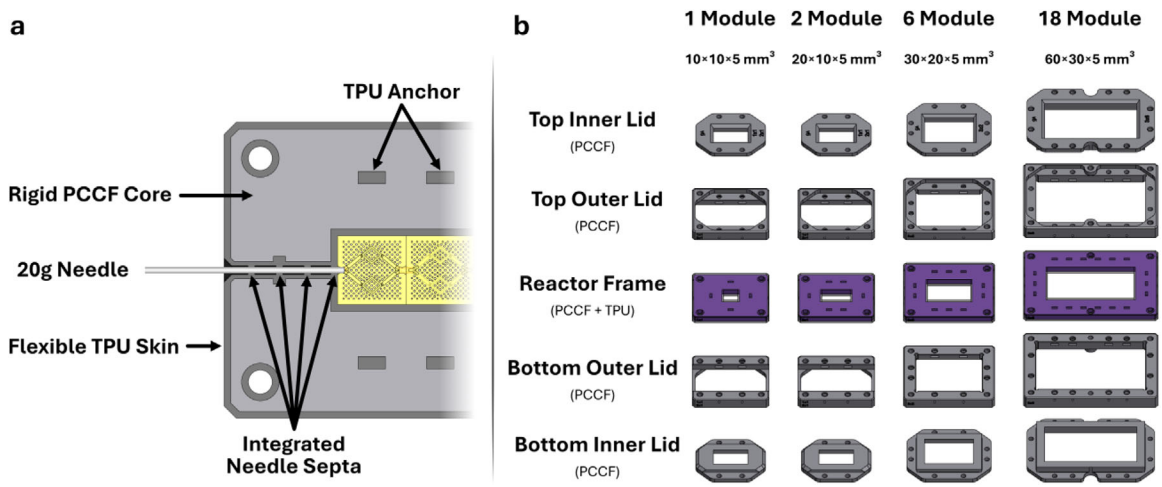

FIGURE 4 | Novel bioreactor design. (a) Cross-section of bioreactor design highlighting rigid PCCF core wrapped with a TPU skin that incorporates the integration of needle septa. (b) Exploded view of bioreactor main components, including top and bottom inner/outer lids and a multi-material central bioreactor frame.

thermoplastic core to provide structure and a soft elastomeric shell for sealing gaskets and needle septa (Figure 4a). Additional information about modifications made to a Prusa XL to enable printing of Shore 60A thermoplastic polyurethane (TPU) filament is provided in SI. Material screening was performed via iterative, qualitative assessment rather than formal quantitative screening to arrive at the final material configuration. Of the materials tested, only polycyclohexylenedimethylene terephthalate (PCTG) and carbon fiber reinforced polycarbonate blend (PCCF) exhibited sufficient interfacial adhesion for use with FilaFlex 60A TPU in multi-material bioreactor printing. Qualitative interfacial adhesion ranking was as follows: polypropylene (PP) < polyvinylidene difluoride (PVDF) < polylactic acid (PLA) < glycol-modified polyethylene terephthalate (PETG) < acrylonitrile styrene acrylate (ASA) < acrylonitrile butadiene styrene (ABS) < PCTG ≈ PCCF. PP and PVDF exhibited severe delamination, preventing completion of the prints. Equivalent multi-material test prints of PLA, PETG, ASA, and ABS were completed successfully, but separated easily from the TPU base. Though both PCTG and PCCF produced multi-material prints with sufficient interfacial adhesion, prototypes manufactured using PCTG were prone to creep upon incubation at 37°C for extended periods. Creep resistance under physiological culture conditions (37°C) was evaluated observationally: constructs fabricated with a PCTG core exhibited visible surface impressions from the glass windows following use, whereas those fabricated with a PCCF core did not. This observation provided clear practical evidence for the superior dimensional stability of PCCF under the thermal and mechanical conditions of long-term culture and informed its selection as the final core material. This material combination has provided longevity across multiple uses of complete bioreactor sets, with cumulative use in perfusion culture exceeding 8 weeks.

The bioreactor design underwent several iterations, culminating in the current version, V5. A full design version history is shown in Figure S9. The full exploded view of the bioreactors utilized in this work is shown in Figure 4b, with parts including the top and bottom inner lid, the top and bottom outer lid, and finally the bioreactor frame. A detailed Bill of Materials (BOM) listing all necessary supplemental components by bioreactor size is shown in Figure S10. mm thick glass slides (1 and 2 module bioreactors) or 3 mm thick acrylic (6 and 18 module bioreactors) were inserted between the central bioreactor frame and each outer lid for optimal sterile and watertight conditions for long-term studies and to permit imaging of hydrogel assemblies in situ.

2.4 | Multi-Module Gluing

Fabrication of multi-module assemblies with interconnected, perfusable open channels required the use of a "glue" to maintain interfacial adhesion and prevent leaking between modules. Constructs were assembled utilizing the same GelMA-AEMA resin with an identical formulation to that used in printing as the photo-crosslinkable glue. Printed modules were washed in sealed petri dishes containing sterile PBS inside a shaking incubator at 100 rpm and 37°C for 24 h to remove excess uncured resin (Figure 5a). Washing media was exchanged for culture media, and incubation continued for an additional 24 h (Figure 5b). Washed modules were loaded into a sterile 2 module bioreactor with the top window removed. 50 µL of GelMA-AEMA resin was injected into the interface between adjacent hydrogel modules using an adjustable pipette (Figure 5c). Perfusion needles were inserted through the bioreactor needle ports and into the tapered inlets of the gels to a depth of approximately 1 mm. The bioreactor was then fully sealed by installing the top glass and capping the needles with Luer lock caps for transport to the incubator (Figure 5d). All screws were torqued using a digital torque driver (TS001, Vanpo, Hefei, CN). An FDM printed photomask was placed over the top window to isolate crosslinking to the interface between the modules. The bioreactor was placed inside an incubator heated to 37°C and perfused with air using a syringe pump at a rate of 500 µL min^{-1} to prevent occlusion of the channel at the glued interface. Bioreactors were perfused with air in the absence of light for approximately 3 min or until excess glue was expelled from the outlet needle. The assembly was then glued via 10 min exposure to 405 nm light using a commercial curing chamber with continuous perfusion of air (Figure 5e). Photobleaching of the media's phenol red chromophore was

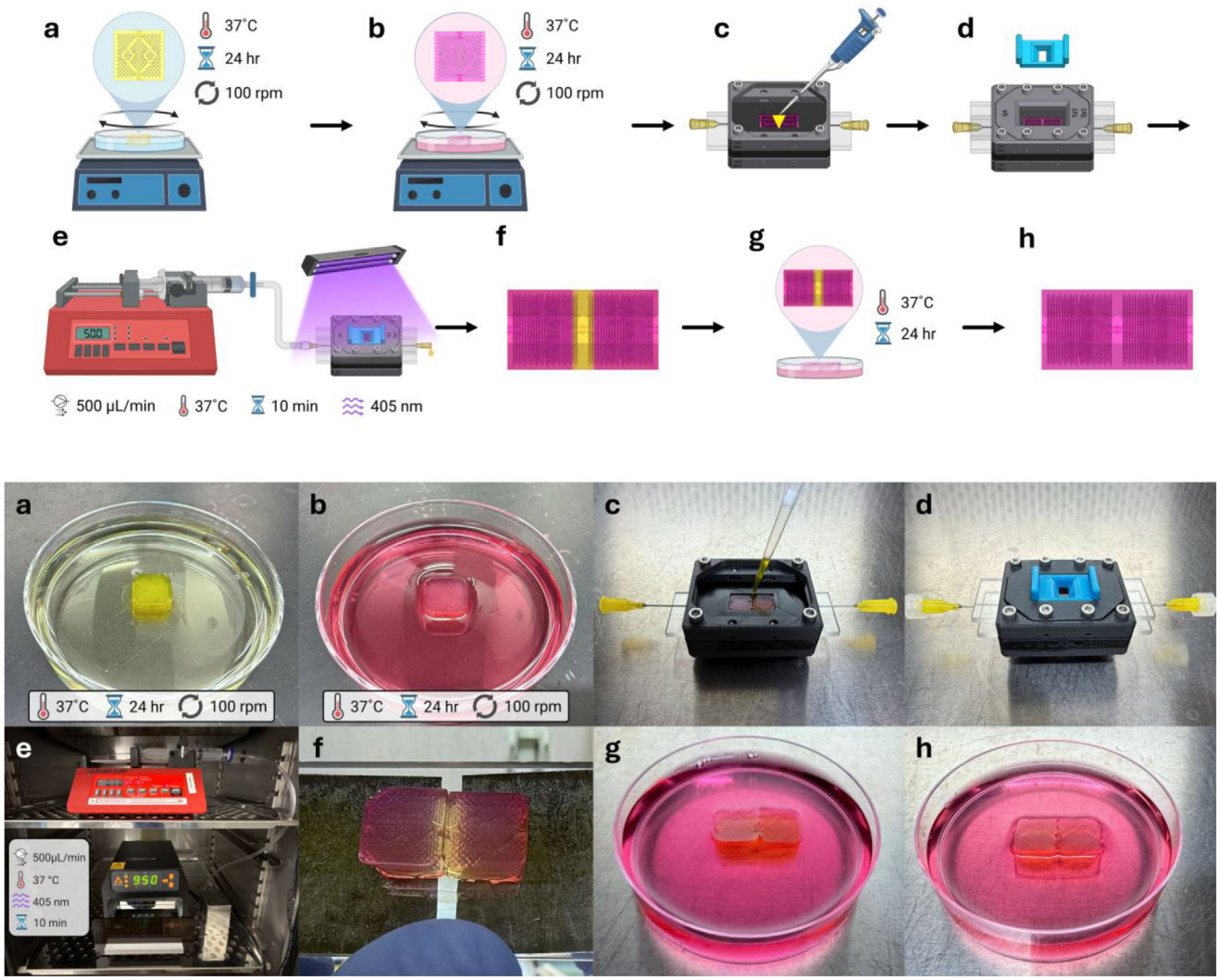

FIGURE 5 | Multi-module gluing procedure. Gluing begins with a wash in (a) PBS and (b) culture media for 24 h each at 37°C while shaking at 100 rpm. (c) Glue is pipetted between the constructs and (d) the bioreactor is sealed to be placed into an incubator for crosslinking, with a photomask installed (blue). (e) Bioreactor is attached to a syringe pump, where air is pushed through the internal geometry to prevent any clogging. (f) Glued construct is removed from the bioreactor and (g) placed into a new dish with fresh media to wash for another 24 h. (h) The construct is now ready for seeding. Created in https://BioRender.com.

utilized as an indicator of complete interface photo-crosslinking (Figure 5f). Glued structures were incubated in fresh culture media for 24 h at 37°C without shaking to facilitate both the removal of excess glue and the diffusion of fresh nutrients back into the hydrogel matrix (Figure 5g). Final washed and glued constructs exhibited uniform pink coloration compared to the initial yellow coloration post-printing (Figure 5h). Larger assemblies with more than two modules were prepared in a similar fashion.

2.5 | Multi-Module Scalability

To demonstrate the feasibility of scaling beyond the 2 module assemblies prepared during the initial gluing experiments, larger acellular constructs measuring $60 \times 30 \times 5$ mm^3 (18 modules) and $30 \times 20 \times 5$ mm^3 (6 modules) were prepared in a similar fashion to that previously described. Hydrogel modules composed of 15 w/v% GelMA-AEMA were photo-crosslinked in PDMS molds measuring $10 \times 10 \times 5$ mm^3. Hydrogels with open lumens measuring ~900 µm were created by photo-crosslinking around 20-gauge needles inserted through ports on the sides of the PDMS molds (Figure S11). These molds allowed for faster creation of single-channel modules for assembly, but printed modules can easily be substituted for the generation of more complex designs. Modules were loaded into assembled bioreactors to generate the desired array, and GelMA-AEMA resin was gently pipetted between each interface (50 µL/interface). After installing the perfusion needles, 1 mm thick FDM 3D printed shims were inserted at opposing ends of the bioreactor to ensure a tight seal at the gluing interfaces. In larger assemblies, shims further aided in perfusion channel alignment by ensuring each outer module edge was flush with the bioreactor wall. The top lid was then installed, with the fasteners torqued. Sealed bioreactors were placed in a 37°C incubator and allowed to thermally equilibrate for 15 min to prevent physical gelation of the glue. Once air

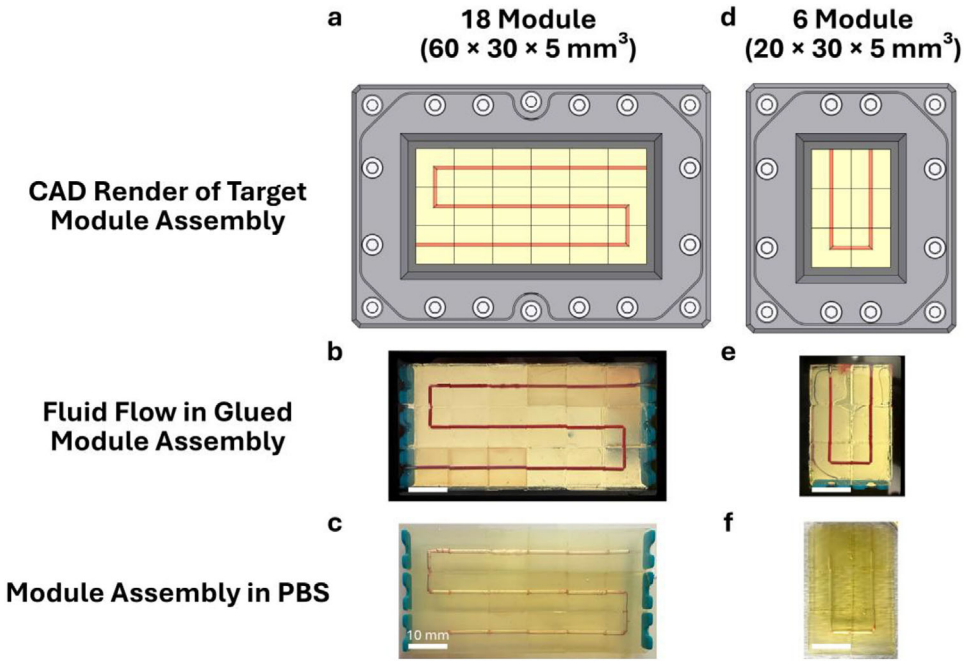

FIGURE 6 | Scalability of approach. CAD model of assembled bioreactor with glued structures inside for (a) 18 module and (d) 6 module structures respectively. Experimental fluid flow results from (b) 18 module and (e) 6 module structures with red dye flowing from the inlet to the outlet with no leaks. (c) and (f) Both structures were removed from the bioreactors into a dish containing PBS, fully intact. All scale bars are 10 mm.

perfusion was initiated, the bioreactors were closely monitored to verify the absence of air leaks at the gel interfaces and to ensure that air was flowing through the entire circuit. Hydrogel constructs were photo-crosslinked for a total of 20 min, with inversion of the bioreactors after the first 10 min. As previously described, air flow was maintained throughout the duration of photo-crosslinking to prevent channel occlusion. Detailed CAD models of modules assembled in their respective bioreactors are shown (Figure 6a,d). Figure 6b,e demonstrate 1 μm red microbead dye fluid flow from inlet to outlet within the sealed bioreactors with no leaks for both 18 module and 6 module structures. A video can be seen in Supporting Information. Fully glued constructs can be removed from the sealed bioreactor and placed into a dish with PBS with no deformation or decrease in sealing ability (Figure 6c,f). Utilization of photo-activated crosslinking chemistries offers superior temporal control over adhesive gelation, eliminating constraints of fixed working times associated with fibrin-based glues and click-chemistries [14, 22]. Our approach to macroscale assembly is unique amongst those leveraging photo-crosslinked modules in that it is compatible with optical 3D printing technologies. Similar approaches rely on physical gelation of methacrylated protein bioinks to maintain extrusion-printed geometry, with subsequent photo-crosslinking of assembled thawed constructs [15]. Due to their dependence on physical gelation, however, such methods are inherently incompatible with optical 3D printing technologies such as PSLA, which offers superior feature resolution and greater print speed since the technique cures entire layers at once. Through the coupling of scalable perfusion bioreactors and photo-crosslinked adhesives, this approach provides the ability to assemble perfusable hydrogel constructs prepared from PSLA printed modules.

2.6 | Seeding Stromal Cells

C3H10T1/2 cells were selected as model stromal cells for this study as they exhibit robust proliferation, high adaptability, and uniform fibroblast-like morphology. Prior to seeding the construct, C3H10T1/2 cells were trypsinized and counted. Cells were then resuspended in Basal Medium Eagle (BME) to create a cellular concentration of 2 million cells mL^{-1}. The glued constructs used for experimentation were prepared for seeding with a pre-soak in media for 24 h (Figure 7a). During seeding, the construct was placed on a thin oxygen-permeable membrane (Figure 7b), while 200 μL of cell suspension was added on top (Figure 7c). For 20 min, the solution was refreshed back to the top as it drained down and through the construct. Next, the construct was rotated 90 degrees and moved to a 60 mm petri dish where it was placed on top of a 200 μL drop of media to keep the construct hydrated (Figure 7d). After 30 min, the construct was reoriented to its flat position, media was added, and it remained in static culture for four days, with a media change on day two (Figure 7e). Constructs were sectioned via an FDM printed jig and a razor blade (Figure S12) and stained with DAPI/Phalloidin. The highly perforated construct geometry resulted in discontinuous cross-sections, rendering thin sectioning via traditional histological embedding methods impractical. When the slice thickness is below the seeding port diameter, sections do not remain intact. To preserve the internal geometry for imaging, cross-sectional thickness was increased utilizing a jig designed for 1 mm sections. A cross-sectional reference of the seeding port geometry is shown in Figure 7f. Sliced ports were observed at Day -4, 4 days prior to perfusion (Figure 7g) and Day 0, the day perfusion starts (Figure 7h). Cells exhibited round morphology prior to full attachment on Day -4 and had increased attachment and

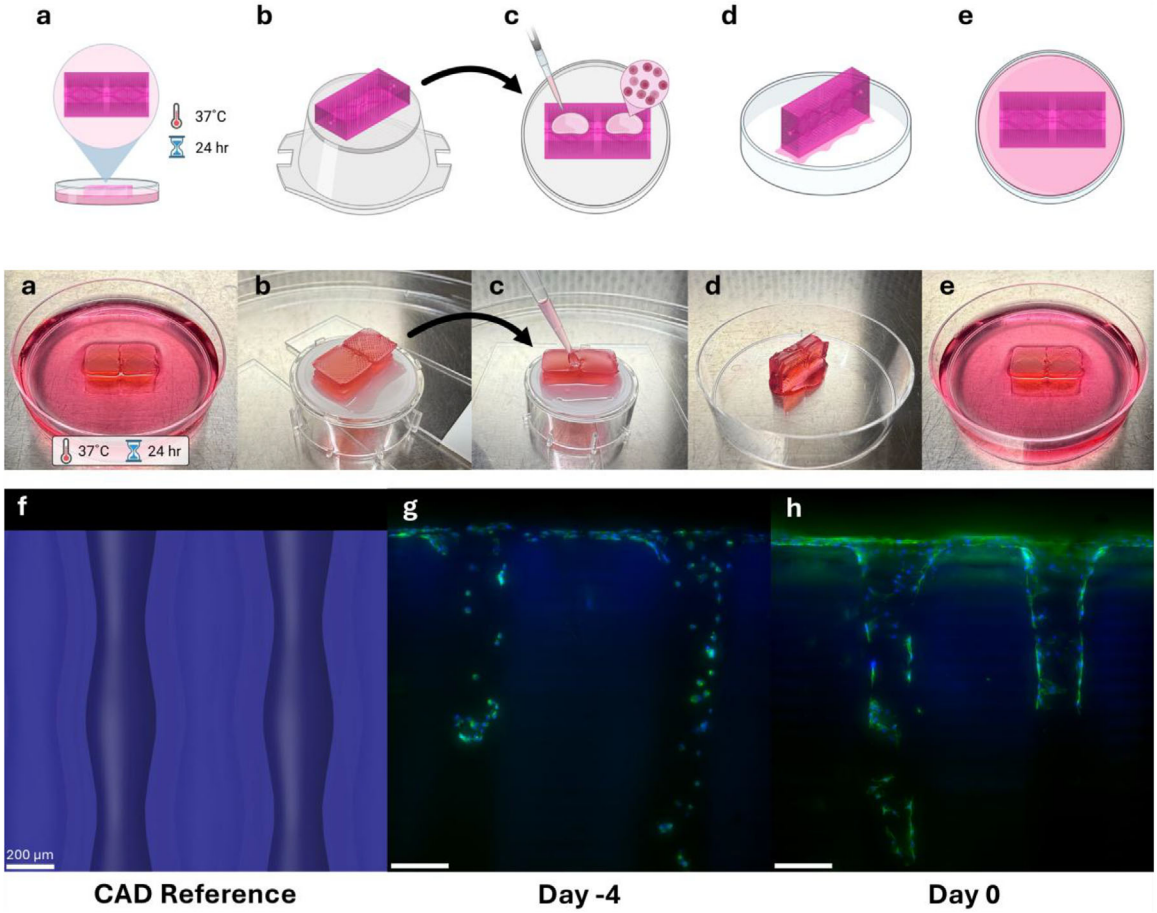

FIGURE 7 | Seeding of stromal cells. (a) Constructs for cell seeding are prepped by soaking in media for 24 h prior. (b) Constructs are placed on an oxygen-permeable membrane, and (c) cell suspension is placed on top and refreshed accordingly. (d) Constructs are placed at 90 degrees to allow cells to coat the seeding ports and refrain from settling to the bottom. (e) Constructs are moved to the original horizontal position and placed in static culture for 4 days prior to perfusion. Cross-section view of seeding port examples of (f) CAD model, at (g) Day -4, and (h) Day 0 stained with DAPI and phalloidin. Scale bars are 200 µm. Created in https://BioRender.com.

proliferation by Day 0, suggesting they would be sufficiently prepared to begin long-term perfusion studies.

2.7 | Cell Growth Over 2 Weeks

As with many tissue engineering solutions presented in the field, key metrics by which to assess new methodologies are their effects on the construct and cells within [38]. In this case, the next step following construct assembly through gluing and cell seeding was to seal the constructs within a bioreactor and perfuse them for up to 2 weeks via a syringe pump. Following perfusion, the constructs were fixed and sectioned into 1 mm slices via the same method described previously. Slices were subsequently washed, stained, and imaged with DAPI and phalloidin accordingly as outlined in the methods section. Representative images of seeded ports for Day 0 (Figure 8a), Day 7 (Figure 8b), and Day 14 (Figure 8c) are shown with DAPI, phalloidin, and a combined overlay, respectively. Images of seeding ports acquired through fluorescence microscopy were imported directly into ImageJ for analysis. A sample going through the full process is shown in Figure 8d. The blue (DAPI) channel was isolated from the rest, where brightness/contrast could be adjusted to maximize nuclei clarity for image processing. The raw Z-stack (Figures S13–S15a) was used to create a Z (max) projection for each port (Figures S13–S15b), and thresholding was completed to convert the image to a binary image (Figures S13–S15c). Watershed separation was induced to cut apart connected components into separate entities. Individual entities (nuclei or clusters of nuclei) were counted using the analyze particles function (Figures S13–S15d), and values were exported to MATLAB for final analysis. In this analysis, a single nucleus was considered to have a diameter of 10 µm, meaning any entities below 10 µm in diameter were not counted as nuclei. Entities larger than 10 µm were counted based on area, with the individual region's area divided by that of a single cell.

Nine fully intact ports were randomly sampled within each of $n = 3$ glued constructs, such that the total ports sampled is equal to $n = 27$ per timepoint. Between Day 0 and Day 14 there was a 68 % increase in nuclei count, with an 11 % increase between Day 0 and Day 7 and a 51 % increase between Day 7 and Day 14 (Figure 8e). Cell counts for sample ports are plotted in Figure 8e grouped by replicate for each timepoint. 95 % confidence intervals (CIs) are plotted for each replicate. Replicates within each timepoint were assessed via ANOVA to verify the absence of

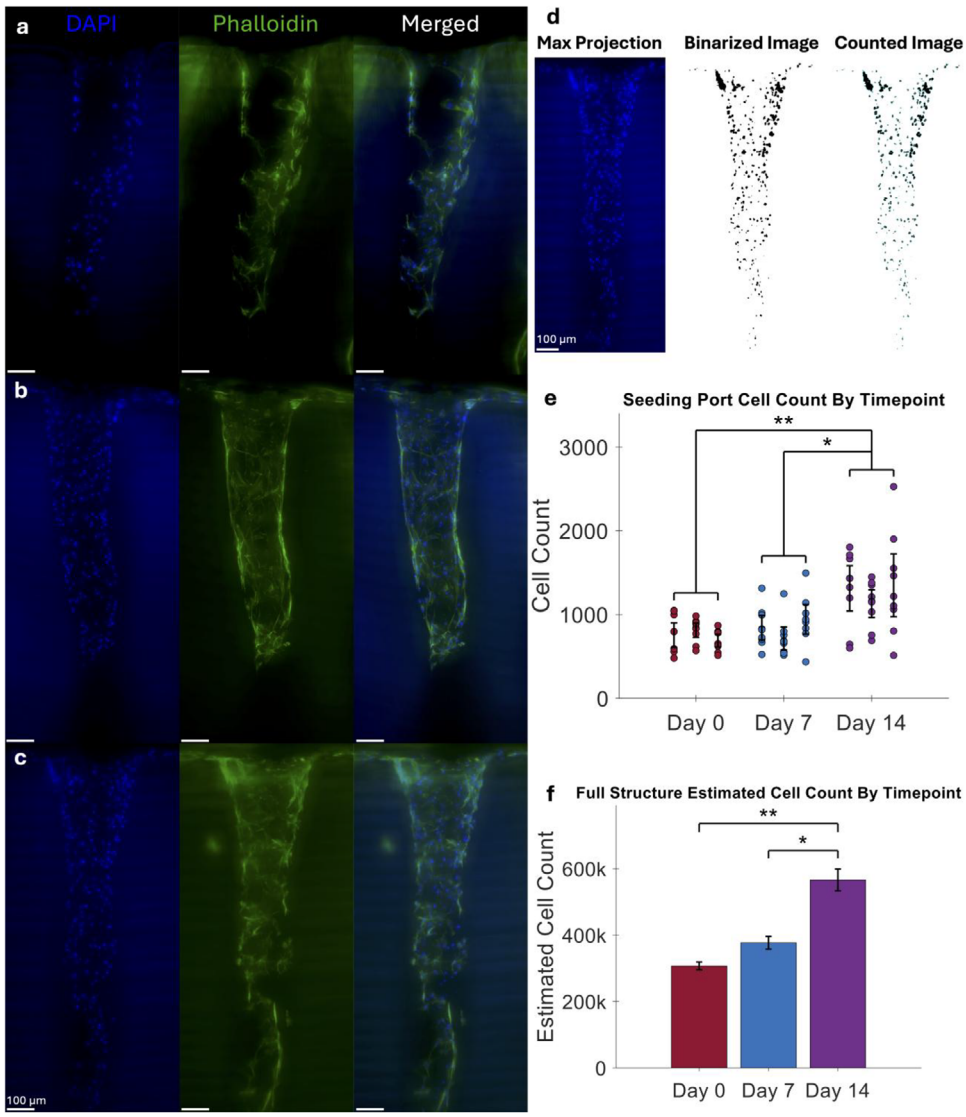

FIGURE 8 | Seeding port result. DAPI, phalloidin, and overlay of (a) Day 0, (b) Day 7, and (c) Day 14 representative seeding ports. (d) Nuclei counting procedure utilized includes max projection from raw Z-stack, binarization of image, and final count. (e) Plot of seeding port cell count by timepoint highlighting an increase in nuclei from Day 0 to Day 14. (*$p < 0.05$, **$p < 0.01$, $n = 27$, ANOVA) (f) Full structure estimated cell count plot for each timepoint based on extrapolated data from seeding ports. (*$p < 0.05$, **$p < 0.01$, $n = 27$, ANOVA) All scale bars are 100 µm.

statistically significant differences. As expected, ANOVA p-values far exceed 0.05 between replicate samples. When comparing between timepoints, a statistically significant difference was observed between Day 0 and Day 14 (ANOVA p-value < 0.05). The limited proliferation between Day 0 and Day 7 can be understood as the result of the cellular microenvironment changing from static to perfusion [39]. Day 0 samples were analyzed prior to perfusion and, accordingly, the cells needed time to adjust to dynamic culture conditions. Due to the absence of statistically significant differences between replicate glued structures, the seeding port cell counts were pooled as replicates in order to estimate the full structure cell count by timepoint (Figure 8f). The estimated cell count for Day 0 was 3.07×10^5, 3.77×10^5 for Day 7, and 5.66×10^5 for Day 14. This represents a 23 % increase between Day 0 and Day 7, a 50 % increase between Day 7 and Day 14, and finally an 84 % increase between Day 0 and Day 14. The discrepancy between percentage increases for individual seeding ports and full structure counts was due to an increase in the number of cell-laden ports as a function of time. Statistical significance of differences between timepoints was verified via ANOVA, with p-values < 0.05. For the purposes of this estimation, only cells within the seeding ports were considered toward the full structure estimate. Cells were visually observed both on the exterior surfaces of the glued structures and within the internal nutrient supply architecture. It should be acknowledged that the total estimated cell count is presented as an underestimate, as these regions were excluded due to the inability to reliably quantify cell coverage across the entirety of the exterior and interior nutrient supply architecture.

During seeding port cross-section analysis, it was observed that cells migrated from the seeding ports toward the exterior faces of the construct. Cells were also observed within the glued constructs' internal nutrient supply architecture. As a visual reminder, the CAD representation of the top view of the printed construct is shown in Figure 9a, and an angled view is depicted in

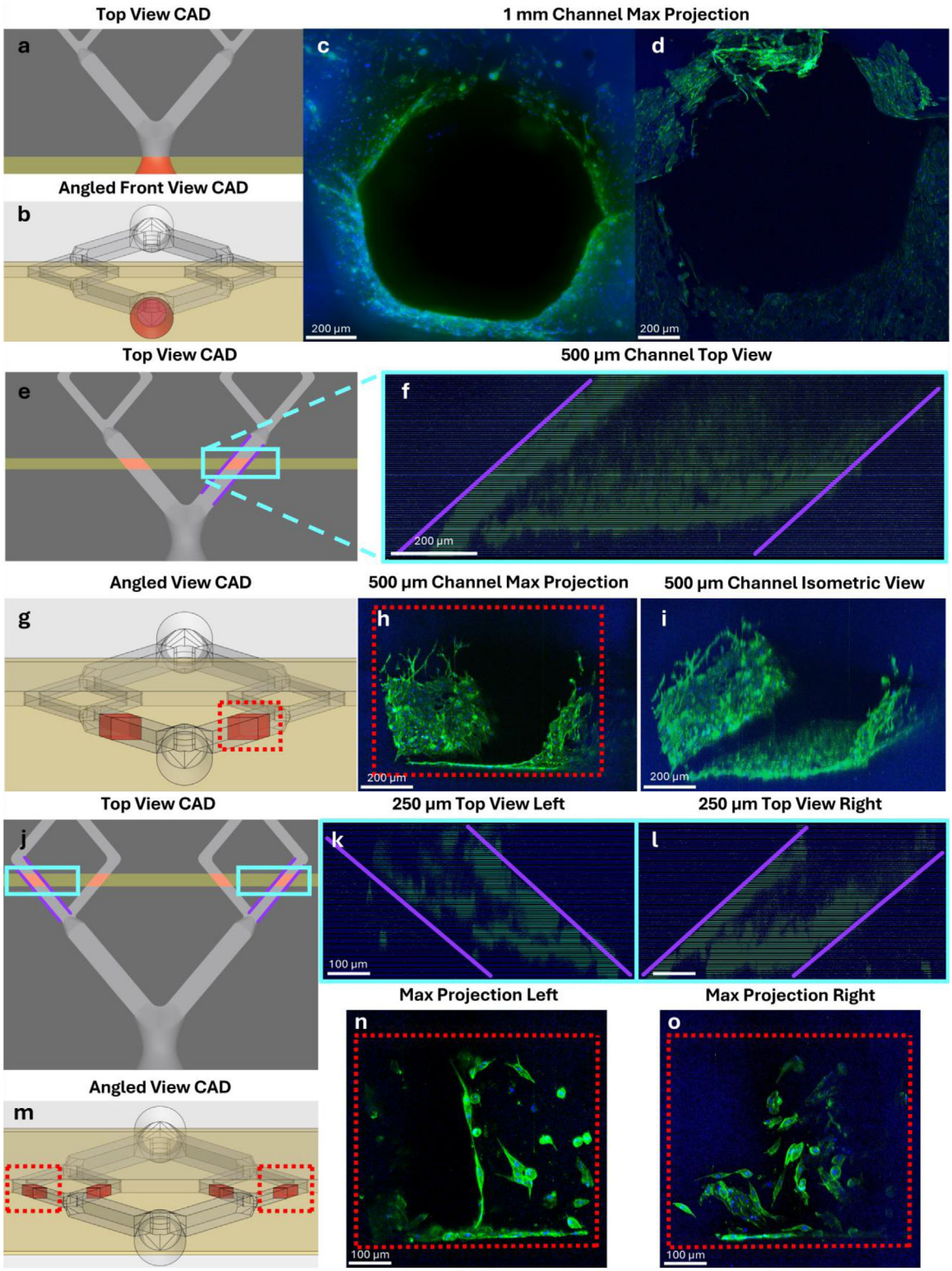

FIGURE 9 | Cell migration within channel network after 2-week long perfusion culture in bioreactors. (a) Top and (b) angled view CAD model highlighting internal geometry size of 1 mm at the inlet. Max projections of sliced sections from this region imaged on (c) fluorescent microscopy and (d) confocal microscopy. (e) Top view CAD in the 500 µm region of branched architecture. (f) Top view created from a 3D reconstruction of a cross-section slice taken from the same region. (g) Angled view CAD of the same region showing (h) max projection and (i) isometric view of 500 µm channel. (j) Top view CAD from the 250 µm region corresponding to the top view of (k) left side and (l) right side channels created from 3D reconstructions. (m) Angled CAD view from the same regions where max projections from (n) left and (o) right are created. Scale bars (c,d,f,h,i) are 200 µm. Scale bars (k,l,n,o) are 100 µm.

Figure 9b, with a focus on the 1 mm wide section of the channel. Conventional fluorescent (Figure 9c) and confocal microscopy (Figure 9d) z-stacks were achieved for the 1 mm slices where a max projection for each could be generated. A cell-lining was observed on the internal channel, as well as a complete coating of the surface face. Moving further into the construct, Figure 9e gives a top-view visualization of the CAD model for the 500 μm wide section of the channels. Z-stacks were obtained from confocal microscopy and utilized to generate a 3D reconstruction of the 500 μm channel, facilitating a top view of this lumen (Figure 9f). The purple fiducial markers help to illustrate the path of the channel as it is angled. An additional CAD view is provided of this section in Figure 9g to illustrate the placement of the geometry pictured in the max projection (Figure 9h) and isometric view (Figure 9i) of the 500 μm open channel. Finally, the presence of cells was observed within the construct's smallest open lumens, measuring 250 μm wide. A top-view CAD is shown at this cross-section (Figure 9j), where the outer two channels were captured in a top-view 3D reconstruction of the left (Figure 9k) and right (Figure 9l) 250 μm lumens. A final CAD angled 250 μm channel view (Figure 9m) is depicted next to the max projections from the left (Figure 9n) and right (Figure 9o) 250 μm channels. The presence of cells in this region provides additional confirmation of both nutrient diffusion through the construct toward the seeding ports and cell proliferation and migration toward the source of food and oxygen flowing through the center of the constructs.

3 | Discussion

While the field of biofabrication has advanced significantly, the generation of organ-scale constructs remains in its infancy due to the inability to meet the metabolic demands of large-sized cellular constructs. To address this challenge, researchers are actively exploring various innovative techniques, each with specific limitations and constraints on their ability to scale up.

3.1 | State-of-the-Art

3.1.1 | Assembly of Cellular Modules

Most commonly, building blocks in the form of cell sheets, cell pellets, spheroids, organoids, and tissue strands have been used to generate high-density macrotissues using methods based on extrusion, magnetic fields, aspiration, and the Kenzan method [13, 40], although each technique has some specific limitations. For instance, extrusion bioprinting suffers from nozzle clogging and mechanical stress-induced cellular damage [41], while magnetic-field-assisted methods must consider nanoparticle cytotoxicity and field non-uniformity [42]. Aspiration-assisted freeform bioprinting needs a support bath, which could reduce cell viability and transparency, making fusion of blocks difficult [43], while the fully automated Kenzan method has limited flexibility, speed, and throughput [44]. Since cell-block volumes $> 1\ mm^3$ require active nutrient perfusion to meet their metabolic demands, strategies to embed endothelialized vasculature or integrate bioreactor-assisted perfusion with macrotissues have been developed. For instance, integration of perfusable networks of endothelialized vasculature within collagen cell sheets enabled researchers to increase the thickness of the microtissue by 10-fold, from ~200 μm to ~2 mm, although scaling up to thicker tissues was not possible [45]. To scale up in 3D, cryo-frozen extrusion bioprinted cell-laden hydrogel modules (XY size ~5 mm) were prefabricated and assembled to generate macrotissues (~1.5 cm) [15]; however, cell encapsulation limits the design complexity and print size of the modules and requires the inclusion of cryoprotective agents.

It is now possible to fuse hundreds of individual spheroids or organoids, typically ~200–500 μm in diameter, into larger macrotissues (~1–2 cm) for specific tissue engineering applications. For instance, cell-laden microbeads (modules) combined with a central lumen were used to generate centimeter-sized bone grafts (1.6 cm length × 2.0 cm diameter), although scale-up would require complex channel networks embedded within the assembly, not currently possible with this technology [18]. In another study, spheroids were aggregated into centimeter-scale lumens similar to an in vivo intestine tubular structure that overcomes the nutrient diffusion limits that typically keep organoids under 3–5 mm [46]. Spatially controlled construction of assembloids using bioprinting (SPOT) can assemble organoids of varying sizes (300–3000 μm) into multi-region assembloids that can exceed 5–8 mm [47]. By fusing four distinct regional organoids (somatosensory, spinal, thalamic, cortical) in series, assembloids of ~1 cm in length and roughly 4× the density of a standard single organoid have been recently reported [48]. To counter diffusion limitations, embedding vascular channel networks within organoid assemblies has also been explored. For instance, sacrificial writing into functional tissue (SWIFT) can assemble organ building blocks into > 1 cm living matrices [49], although increasing the cell density in bioinks would require more viscous inks, which in turn could decrease cell viability. Human-sized, tibia-shaped scaffolds measuring 42 × 21 × 10 mm (~8820 mm^3) were constructed via inkjet printing of cell-laden hydrogels within 3D printed PCL frames. However, without an internal channel network to actively perfuse nutrients, hypoxia-induced necrosis remains a key challenge to scale up [50]. A high-throughput integrated tissue fabrication system [51] demonstrated the fabrication of 1 cm^3 cartilage constructs containing approximately 600 chondrogenic spheroids in under 40 min. This approach similarly faces significant challenges to scaling up to larger sizes due to a lack of integrated media perfusion. Bioprinting-assisted tissue assembly (BATA) showed that it is possible to assemble heart tissue modules in a manual or semi-automated manner. However, large-scale constructs are prone to falling apart under their own weight during the maturation phase, especially without complex temporary supportive frameworks, and cardiac tissue exceeding 200 μm in thickness suffers from necrotic cores [52, 53]. Bio-pick, place, and perfuse (Bio-P3), an integrated robotic platform, was developed to pick microtissue parts and stack them in a layer-by-layer manner [54]. Since individual microtissues are designed with integrated lumens, when stacked, these lumens are precisely aligned to form continuous internal channels, allowing for active perfusion of nutrient-rich media through the center of the growing microtissue. Using this setup, a tissue of ~410 mm^3 was fabricated. Thus, most assembled macrotissues are currently limited to ~1 cm sizes, due to the high metabolic demands of high-density cells, an absence of internal perfusable channel networks, and many method-based constraints while handling living cells or organoids.

3.1.2 | Assembly of Cell-Free Pre-Printed Modules

To address the various challenges related to bioprinting living cells, pre-printed bioink blocks can be assembled into macrostructures, and cells can be seeded post-assembly, thus decoupling cells from often cell-unfriendly printing processes. In one study, a commercial printer was used to print modular collagen units (1 cm × 1 cm × 1.5 mm) and then manually assembled into organ-scale constructs such as planar sheets (6 cm × 11 cm), 3D soccer ball or 3D model of a full-size human heart using more than 60 units, although fragility of the final structure and cell seeding on surfaces of these 2.5D sheet modules limits its utility for generation of large 3D tissues [14]. In another study, a number of millimeter-sized cages made out of beta-tricalcium phosphate ceramic were printed, and cells were incorporated post-fabrication [55]. Damage during the physical interlocking of cell-loaded blocks and an absence of internal perfusable vascular networks are key challenges to making larger implants with this technology. To prevent damage during assembly, cell-friendly gluing of smaller extrusion-printed channels has been used to make larger branched channel structures [56]. The MultiCUBE platform allows modular assembly of L-shaped frames with custom hydrogel solutions to potentially guide 3D tissue morphogenesis. Although the frame design allows hydrogel solutions to be trapped using manual pipetting, frame size is limited to ∼2.5 mm to prevent dripping, and without a connected vascular supply between units, scaling up remains difficult [21].

3.1.3 | Our Work: Assembly of Cell-Seeded, Perfusable 3D Printed Hydrogel Modules

In this work, modular assembly of acellular GelMA-AEMA modules combined with simple cell-seeding is used to circumvent the contrasting relationships between print volume, print resolution, and construct viability during and post printing. Each module of 500 mm^3 features an array of open, undulating channels, offering more surface area for enhanced seeding efficiency while simultaneously providing seeded cells greater access to the full volume of the matrix. Furthermore, precise alignment of inlet and outlet macro channels between adjacent modules, achieved via slight compression of gels against the bioreactor walls, ensures media perfusion throughout the entire assembly during perfusion culture. Assembly of modules with an internal network of multiscale, perfusable channels ensures cell viability both within each module and across the macroscale assembled construct. Since cell seeding is decoupled from the printing process, longer printing times (∼90 min per module), often necessary to make modules with complex internal channel topology, do not have any impact on cell viability. This is an advantage as compared to current bioprinting methods, where the use of cell-laden bioinks enforces strict processing conditions to maintain high cell viability and prevent sedimentation during printing [57, 58]. For instance, printing a volume of ∼1 cm^3 can expose cells to harsh processing conditions for long durations (∼3 h) for PSLA and ∼30 h for extrusion bioprinting, while the cell viability window is typically ∼1 h. Cell seeding is not limited by light scattering, a challenge during PSLA-based bioprinting [59, 60]. Additionally, handling and sterilization become relatively straightforward due to the exclusion of cells during the printing process.

New multi-material perfusion bioreactors facilitate both macroscale assembly and long-term culture of cell-seeded modules. The 3D printed bioreactor design reduces manufacturing time and can accommodate larger module assemblies in custom configurations. Modules can be printed, stored until use, and rapidly assembled based on target tissue size and/or study design. Scaling is accomplished by leveraging intuitive LEGO-like assembly in which stacking of modules offers a high degree of geometric freedom without the need for specialized equipment. Modules can be stacked on or beside each other to render large-sized constructs using manual placement or existing automation setups. In our printing process, the edges of the modules are intentionally slightly under-cured to retain a fraction of unreacted functional groups. Additionally, the modules are photo-crosslinked in situ but not subjected to any additional UV or thermal post-curing step, which is commonly applied in DLP workflows specifically to increase conversion of remaining photo-crosslinkable groups at the surface and in the bulk. As a result, a finite fraction of methacrylate/methacrylamide functionalities remains available after printing, consistent with reports that significant populations of unreacted double bonds persist in DLP-printed acrylate networks in the absence of post-curing [61]. When GelMA-AEMA is subsequently applied as an adhesive phase, these residual groups can form covalent bonds across the interface. The diffusion of GelMA resin into pre-crosslinked GelMA scaffolds has been systematically investigated across a range of macromer concentrations. In 10 wt/v% GelMA scaffolds, only very limited resin penetration was observed [15]. In this work, GelMA-AEMA scaffolds were formulated at a higher concentration of 15 wt/v%, further restricting resin diffusion due to increased steric hindrance. Given that incubation times prior to photo-crosslinking were shorter than those used by Luo et al., it is unlikely that interpenetration or a mechanical interlock contributes significantly to interfacial adhesion of modules. In the current study, the mechanical robustness of the interface was not quantitatively assessed. However, throughout the experiments, no signs of delamination or structural separation were observed, even under continuous perfusion flow. In longer term perfusion culture, it is expected that remodeling of modules with cell-deposited matrix will influence the interfacial properties. In this work, channel patency in multi-module assemblies is demonstrated via perfusion of dye solutions and microbead suspensions. Although maximum internal pressure inside the module was not directly measured, the system was subjected to a maximum flow rate of approximately 665 μL min^{-1} prior to cellular introduction, which was determined to be the upper bound for maintaining wall shear stress within the clinically relevant range of ≤1 dyne cm^{-2} [28–30]. No evidence of leakage or delamination was observed at this flow rate. For long-term perfusion culture, a flow rate of 3.33 μL min^{-1} was selected, which delivers approximately five construct volume equivalents per day while remaining well below the shear stress threshold of 1 dyne cm^{-2}. Together, these conditions demonstrate that the adhesive interface maintains structural integrity across the full range of flow rates relevant to the intended application. Assembly of modules generates sizes that far exceed the typical build volumes associated with a particular method. As proof of concept, assemblies of 18 modules (∼9000 mm^3) are glued, assembled, and perfused, serving as a framework to make macrotissues approaching clinically relevant sizes. Beyond

PSLA, our modular assembly strategy can be extended to other printing modalities such as extrusion-based methods, which offer a wider range of bioink materials, or volumetric additive manufacturing that can decouple printing speed and volume.

3.2 | Limitations and Future Work

The primary aim of this study was to establish a viable assembly method and perfusion platform capable of supporting the rigorous future investigation of modular tissue constructs, an area in which robust, accessible experimental systems are critically needed. The methods developed herein also highlight some limitations that could provide a foundation for subsequent studies related to long-term tissue maturation and organotypic function. For instance, cells are visible within the branched channel network due to their migration during initial static cell culture. To prevent co-inhabitation of seeded cell types, the inlets of modular assemblies can be temporarily blocked during cell seeding in future work. By customizing seeding ports, spheroids or organoids can also be seeded, paving the way toward tissues with clinically relevant cell densities. Future studies may also focus on rigorous characterization of the effects of seeding port count, dimensions, geometry, and array density to quantify their effects on cell seeding efficiency. Here, only planar branched channel networks are used, limiting the height to 5 mm. Future experiments could utilize complex 3D topologies spanning deeper into the modules, allowing modules of increased height to be assembled into macroscale constructs. Our assembly approach relies on a single fluidic path per perfusion channel with one inlet and one outlet per module. This limitation may restrict compatibility with models featuring less regular or more highly branched perfusion networks due to increased risk of trapped resin or bubbles resulting in undesirable occlusions. It may be partially mitigated through the application of generative design and flow simulation to create models with more complex internal geometry while maintaining even, distributed flow. Contemporary literature utilizes 1–2-week time points for validation of seeding and culture method efficacy, and served as the basis for these time points. Extending the perfusion culture duration to 4–6 weeks can provide insights about the tissue maturation process. It is important to note that long-term cell studies will require systematic characterization of the physical properties of assemblies, including mechanical limits of glued interfaces, perfusion stability over time, and pressure limits associated with flow rates. Though not discussed in this work, the effects of cellular ECM remodeling must also be studied to elucidate the impact on long-term integrity of modules and glued interfaces. Further, rigorous quantitative characterization of the bioreactor platform, including pressure tolerance, creep, and interfacial adhesion, will be required to ensure the maintenance of sterile conditions during extended perfusion culture. Although this study only focused on a single cell type and a single biomaterial, this workflow can be extended to incorporate multiple bioinks, cell types, and module configurations. Gluing of modules fabricated from different acrylated or methacrylated biomaterials in varying proportions could be used to optimize scaffold modulus according to cell type. Seeding of vascular endothelial cells into the branched channel network can be combined with stromal cell seeding within ports to characterize the effects of multi-cellular interactions on tissue maturation. To achieve this, media formulations, perfusion rates, and cell seeding sequence and concentrations must be optimized. Future work could establish relationships between endothelialization conditions, channel network architecture, and tissue maturation. Longer term, transition away from model cell lines toward clinically relevant induced pluripotent stem cells (iPSCs) will be a critical step in the progression of this platform toward translational applications. Successful integration of iPSC-derived cell types would substantially enhance the physiological fidelity of the constructs generated and would represent an important milestone in the development of patient-specific tissue engineering strategies within this framework. It is anticipated that with increasing modular assembly scale comes a greater risk of encountering several interconnected scaling challenges. These include elevated backpressure arising from increased pressure gradients across larger assemblies, changes to nutrient and oxygen transport as the total diffusion area scales, and potential reductions in the mechanical stability of the overall construct. Computational approaches will play an important role to inform the design of larger assemblies prior to empirical testing. Additionally, the development of appropriate live perfusion imaging methodologies will present their own technical challenges at scale, particularly with respect to maintaining focal plane registration in the Z-axis during imaging of large 3D constructs. Our macroscale assembly platform represents a starting point to build upon, which can help bridge the gap between current fabrication limits and on-demand clinically relevant large-scale grafts. This would require the demonstration of long-term organotypic maturation, use of relevant cells (iPSCs), thrombus-free perfusion culture, and surgical implantation feasibility. Overall, this work presents an accessible approach to the generation of large-scale tissue constructs by balancing critical tradeoffs between print volume, design complexity, and cell viability, offering the potential to help broaden participation in this area of research.

4 | Conclusions

This work features an alternative approach to fabricating large, perfusable constructs from smaller, optically printed hydrogel modules with two sets of embedded hollow features. This method leverages macroscale assembly and asynchronous printing of modules to circumvent a ubiquitous challenge in PSLA: the inherent compromise between print area and feature resolution. This allows printers optimized for high resolution printing of hydrogels to be used to fabricate structures which far exceed their native build volumes while maintaining open, perfusable lumens. Also reported is a novel use of cell seeding ports in PSLA printed hydrogels to facilitate higher seeding efficiency and enhanced gel colonization as an alternative strategy to overcome print time limitations associated with traditional bioprinting with encapsulated cells. Finally, the design and fabrication of new multi-material perfusion bioreactors, which facilitate both macroscale assembly and long-term culture of cell-laden hydrogel structures, is reported. The unique design of the perfusion bioreactors reduces manufacturing time and supports increased scaling to accommodate large hydrogel constructs.

5 | Materials and Methods

5.1 | GelMA-AEMA Synthesis and Preparation

Gelatin type B was obtained from Rousselot (Ghent, Belgium). Methacrylic anhydride, 1-ethyl-3-(3-(dimethylamino)propyl)carbodiimide (EDC), and deuterium oxide (D_2O) were purchased from Sigma–Aldrich (Diegem, Belgium) and used without further purification. Dimethyl sulfoxide (DMSO, 99.85 %) and N-hydroxysuccinimide (NHS, 98 %) were sourced from Acros (Geel, Belgium). 2-Aminoethyl methacrylate hydrochloride (AEMA·HCl) was supplied by Polysciences (Conches, France), whereas the lithium 2,4,6-trimethylbenzoylphenylphosphinate (Li-TPO) was synthesized in-house based on a previously described procedure [62]. Dialysis membranes (Spectra/Por, MWCO 12 000–14 000 Da) were obtained from Polylab (Antwerp, Belgium).

The methacrylation of the primary amines in gelatin type B was carried out as previously described [35]. In brief, 100 g of gelatin B (corresponding to 38.5 mmol amine groups) were dissolved in 1 L of phosphate buffer (pH 7.8) at 40°C under continuous mechanical stirring, after which methacrylic anhydride (14.34 mL, 96.25 mmol, 2.5 molar equivalents) was added and allowed to react for 1 h. The mixture was subsequently diluted with 1 L of double-distilled water and purified by dialysis against distilled water (MWCO 12 000–14 000 Da) for 24 h at 40°C with five water exchanges. The resulting solution was then frozen and lyophilized (Christ freeze-dryer Alpha I-5, Osterode am Harz, Germany) to yield the methacryloyl-functionalized gelatin (GelMA).

Fully functionalized GelMA (10 g, 10.042 mmol carboxylic acid groups) was dissolved in 300 mL of dry DMSO at 50°C under an inert atmosphere with reflux conditions. Once complete dissolution was achieved, EDC (1.00 g, 5.21 mmol, 0.5 equivalents) and NHS (0.90 g, 7.82 mmol, 0.75 equivalents) were added simultaneously along with 50 mL of dry DMSO and allowed to react for 30 min. Subsequently, 2-aminoethyl methacrylate hydrochloride (AEMA·HCl; 0.86 g, 5.21 mmol, 0.5 equivalents) and 4-tert-butyl catechol (17.32 mg, 0.1 mmol, 0.01 equivalents) were introduced together in 50 mL of dry DMSO. The mixture was kept under an inert atmosphere, protected from light, and stirred overnight at 50°C. After completion, the solution was precipitated into a tenfold excess of cold acetone, and the solid product was collected by filtration on a glass filter (no. 4). The precipitate was redissolved in double-distilled water, dialyzed against distilled water (MWCO 12 000–14 000 Da) for 24 h at 40°C with five water exchanges, then frozen and lyophilized to yield the final gelatin derivative, hereafter referred to as GelMA-AEMA.

The degree of substitution of gelatin was determined by ^{1}H NMR spectroscopy (Bruker WH 500 MHz, Billerica, MA, USA) using D_2O as solvent at 40°C. Characteristic resonances corresponding to methacrylamide groups in GelMA (δ = 5.50 ppm (s, 1H) and 5.70 ppm (s, 1H)) or methacrylate groups in GelMA-AEMA (δ = 6.20 ppm (s, 1H) and 5.80 ppm (s, 1H)) were quantified relative to the integration of non-reactive aliphatic protons from Val, Leu, and Ile residues (δ = 1.01 ppm, 18H). The degree of substitution was calculated from the ratio of these integrals according to the amino acid composition of the gelatin.

$$DS_{MA}\,(\%) = \frac{0.384\,\frac{\frac{(I_{5.5}+I_{5.7})}{2}}{I_{1.0}}}{n_{NH_2}}\,x\,100 \quad (1)$$

$$DS_{AEMA}\,(\%) = \frac{0.384\,\frac{I_{6.2}}{I_{1.0}}}{n_{COOH}}\,x\,100 \quad (2)$$

The crosslinking kinetics of the modified gelatin samples were evaluated using a Physica MCR-301 rheometer equipped with a parallel plate geometry (upper plate diameter of 25 mm). A 300 µL solution of GelMA or GelMA-AEMA at 15 wt/v% in double-distilled water, containing 2 mol% Li-TPO photoinitiator relative to the total amount of double bonds, was loaded between the parallel plates set at a 0.3 mm gap. The sample edges were trimmed and sealed with silicone grease to prevent drying. Measurements were performed at 37°C under constant UV-A irradiation (25 mW cm^{-2}, 400–500 nm, EXFO Novacure 2000) while applying an oscillatory strain of 0.1 % at 1 Hz frequency. The evolution of the storage (G′) and loss (G″) moduli was continuously monitored as a function of time throughout the photo-crosslinking process.

Post-print swelling was measured using hydrogel samples bearing the same external dimensions as printed modules (10 × 10 × 5 mm^3), which were prepared from photo-crosslinking 500 µL of either GelMA or GelMA-AEMA resin in PDMS molds. Resin composition was identical to that used for printed GelMA-AEMA samples, with 15 wt/v% protein in each resin. Samples were photo-crosslinked in an LED curing chamber (B9A-LCB-010, B9 Creations, Rapid City, SD, USA) for 10 min and weighed after demolding. Excess swelling was induced by incubating molded samples in PBS for 24 h at 37°C with 100 rpm shaking. Swollen samples were weighed again after carefully removing excess fluid from their surfaces. Excess mass swelling ratio (%) was calculated using the equation below, where the sample mass after photo-crosslinking (m_p) and the sample mass after swelling (m_s) were used. Note that a swelling value of 100% would indicate the absence of post-print swelling.

$$Excess\ Mass\ Swelling\,(\%) = \frac{m_s}{m_p} \times 100 \quad (3)$$

5.2 | Vat Fabrication

The printing vat was constructed with a polystyrene Falcon brand 60 mm × 15 mm petri dish (Corning, Corning, NY, USA) with 3.5 grams of Sylgard 184 poly(dimethylsiloxane) (PDMS) (Ellsworth Adhesives, Germantown, WI, USA) cured to the bottom of the dish. The PDMS was poured into the Falcon petri dish, degassed in a vacuum to remove air bubbles, and heat cured at 60°C overnight.

5.3 | Glass Coverslip Methacrylation

Glass slides (25 mm × 75 mm × 1 mm, Fisher brand) were precleaned with piranha solution (H_2SO_4 and H_2O_2; 7:3), stirred

for 30 min, washed with ethanol and DI water until reaching a neutral pH, and dried in a vacuum oven at 65°C. The glass slide surface was further functionalized by 3-(trimethoxysilyl)propyl methacrylate (TMSPMA; Sigma–Aldrich) and toluene (Sigma–Aldrich) (9:1) at 50°C and then washed in ethanol and DI water and dried.

5.4 | CAD Design and Slicing

Models were designed using a combination of Shapr3D (Shapr3D Zrt, Budapest, Hungary) and Autodesk Inventor (Autodesk, Inc., San Francisco, CA, USA). Photomask slices were generated with Formware 3D (Formware B.V., Amsterdam, The Netherlands). Post-processing of photomasks to reduce the bit depths from 8 to 1 was performed using ImageMagick.

5.5 | Design and Fabrication of a PCCF/TPU Perfusion Bioreactor

5.5.1 | Bioreactor Materials Screening

Rigid thermoplastic filament types were screened for interfacial adhesion to prevent delamination of bioreactors. Several common 3D printing filament types were selected for testing including Prusament polylactic acid (PLA) (Prusa Research a.s., Prague, Czech Republic), Fusion Filaments acrylonitrile butadiene styrene (ABS) (Fusion Holdings LLC, Maryland Heights, MO, USA), Prusament acrylonitrile styrene acrylate (ASA) (Prusa Research a.s.), IC3D glycol-modified polyethylene terephthalate (PETG) (IC3D, Hilliard, OH, USA), Fiberlogy glycol-modified polycyclohexylenedimethylene terephthalate (PCTG) (Fiberlab S.A, Brzezie, Poland), Formfutura polypropylene (PP) (FormFutura B.V., Nijmegen, The Netherlands), 3DXTech polyvinylidene difluoride (PVDF) (3DXTech, Grand Rapids, MI, USA), and Prusament carbon fiber reinforced polycarbonate blend (PCCF) (Prusa Research a.s.). Interfacial adhesion was tested by printing $10 \times 10 \times 5$ mm^3 slabs of each material on top of an identically sized slab printed in Recreus Filaflex Pro 60A thermoplastic polyurethane (TPU) (Recreus Industries S.L., Alicante, Spain). Samples were assessed qualitatively based on the presence of warping or self-delamination and the resistance to mechanically induced delamination.

5.5.2 | Bioreactor Manufacturing and Assembly

FDM 3D printed parts, including bioreactor frames and lids, were made with an enclosed 5 toolhead Prusa XL (Prusa Research a.s.) using a combination of PCCF and TPU. Full print settings and material profiles are available in 3MF file format (3MF with filament profiles and print settings is available at https://github.com/psomanlab/modular-assembly). Minor modifications to the printer were required to facilitate the reliable printing of PCCF and Shore 60A TPU. A full list of modifications can be found in Supporting Information and in the GitHub repository.

Small bioreactors for 1 and 2 module(s) ($10 \times 10 \times 5$ mm^3 and $20 \times 10 \times 5$ mm^3), respectively, utilized 3 mm thick microscope slides for the top and bottom windows. Larger bioreactors for 6 and 18 module assemblies ($30 \times 20 \times 5$ mm^3 and $60 \times 30 \times 5$ mm^3), respectively, instead used 3 mm thick laser-cut acrylic windows due to the limited availability of affordable glass with suitable dimensions. Bioreactor lids were designed in two parts to allow removal of either the top or bottom window for access to the gels without full bioreactor disassembly. Outer lids were secured to the multi-material bioreactor frame using M3 socket head screws and hexagonal nuts. Inner, window-retaining lids were secured to the outer lids using M3 screws and embedded square nuts. An adjustable digital torque driver was used to tighten all M3 screws to 0.15 N·m.

5.6 | Sterilization

Sterile PBS was added to GelMA-AEMA, and the resulting solution was sterilized in a UV chamber (Skin+Act, Chatsworth, CA) for 1 h. Stock solutions of Li-TPO and tartrazine were filter sterilized using 25 mm diameter 0.2 µm SFCA filters prior to addition to the sterilized GelMA-AEMA solution. Before each print, the resin vat and printing platform were wiped with anhydrous ethanol. Bioreactor parts were wiped with 70 % ethanol, separated into petri dishes, sealed with a layer of Duraseal (Diversified Biotech, Dedham, MA) and Parafilm (Amcor, Zurich, Switzerland), and placed in a UV chamber for 2 h. Prior to experimental start, sterilized bioreactor parts were moved into a BSC and sprayed again with 70 % ethanol.

5.7 | Cell Culture

According to standard cell culture protocol, mouse embryonic fibroblast cells (C3H10T1/2, ATCC, Manassas, VA, USA) were cultured and passaged at 37°C with 5 % CO_2. Basal Medium Eagle (BME, Gibco, Grand Island, NY, USA) containing Earle's Salts and supplemented with 1 % penicillin-streptomycin (Gibco), 1 % Glutamax (Gibco), and 10 % fetal bovine serum (FBS, GeminiBio, West Sacramento, CA, USA) was used. For passaging, 0.05 % Trypsin-EDTA was used (Gibco).

5.8 | Cellular Seeding

Prior to seeding the construct, C3H10T1/2 cells were trypsinized and counted. Cells were then resuspended in BME to create a cellular concentration of 2 million cells mL^{-1}. The glued constructs used for experimentation were prepared for seeding with a pre-soak in media for 24 h. During the seeding procedure, the construct was placed on a thin oxygen-permeable membrane (0.4µm Nunc PC Cell Insert, ThermoFisher Scientific), while 200 µL of cell suspension was added on top. The solution was refreshed back to the top as it drained down and through the construct one time per minute for a total of 20 min. Next, the construct was rotated 90 degrees and moved to a 60 mm petri dish, where it was placed on top of a 200 µL drop of media to keep the construct hydrated. After 30 min, the construct was moved to its original flat position, media was added, and it remained in static culture for four days, with a media change on day two.

5.9 | Perfusion

The bioreactors were connected to an 8-channel syringe pump (NE-1800 Eight Channel, New Era, Farmingdale, NY, USA) to perfuse BME through each syringe at a speed of 3.33 μL min^{-1} for up to 2 weeks.

5.10 | Fluorescent Staining

5.10.1 | Flow Visualization

1 μm red fluorescent microbead dye suspension (Polysciences Inc., Warrington, PA, USA) was diluted 2:1 with DI water. 2 MDa FITC-Dextran (Sigma) was diluted to 1 mg mL^{-1} with DI water.

5.10.2 | Live/Dead

To test cellular viability in cell-laden constructs at each timepoint, live cells were stained with Calcein-AM (1:2000 dilution, Life Technologies, Waltham, MA, USA), and dead cells were stained with ethidium homodimer-1 (1:500 dilution, Life Technologies). Stained constructs were placed in the incubator for 45 min and then washed with PBS three times before imaging. Brightfield and fluorescence images were captured using a Leica Thunder microscope (Leica, Wetzlar, Germany).

5.10.3 | DAPI and Phalloidin

To fix cells, the constructs were soaked in a 4 % paraformaldehyde–PBS solution (Thermo Fisher Scientific, Waltham, MA, USA & Gibco) for 24 h at 4°C. Following fixation, the constructs were cut into 1 mm slices using an FDM printed jig and a razor blade. Slices were placed into a petri dish and washed three times with PBS. To permeabilize the cells within the construct, the slices were soaked in 0.2 % (v/v) Tween–20–PBS solution (Thermo Fisher Scientific) at room temperature for 20 min. Afterward, the sample was washed three times with PBS. Cells were stained with 1:200 PBS-diluted Alexa Fluor 488 phalloidin (Thermo Fisher Scientific) and incubated at room temperature for 40 min, covered with aluminum foil to decrease exposure to light. After incubation, the sample was washed three times with PBS. Next, the cells were stained with 1 μg mL^{-1} PBS-diluted DAPI (Thermo Fisher Scientific) and incubated for 20 min at room temperature, covered with aluminum foil. Finally, the slices were washed with PBS three times and imaged using a Leica Thunder fluorescent microscope and Leica DMi8 confocal microscope (Leica, Wetzlar, Germany).

5.11 | Cell Count Analysis

Image processing was completed in ImageJ, and numerical analysis was computed in MATLAB (MathWorks, Natick, MA, USA).

5.12 | Statistical Analysis

Unless otherwise stated, numerical data were processed using MATLAB to calculate mean, standard deviation, and 95 % confidence intervals. MATLAB was used to generate graphs using these computed metrics. The significance of differences was assessed via Welch's *t*-tests and one-way analysis of variance (ANOVA) using GraphPad Prism 10.3.0 (Dotmatics, Boston, MA, USA), with *p*-values less than 0.05 accepted as statistically significant.

Author Contributions

Z.J.G. performed writing – review and editing, writing – original draft, visualization, validation, supervision, software, project administration, methodology, investigation, formal analysis, data curation, and conceptualization. D.F. performed writing – review and editing, writing – original draft, visualization, validation, supervision, software, project administration, methodology, investigation, formal analysis, data curation, and conceptualization. B.V.D. performed writing, review, and editing, data curation, validation, and visualization. J.G. performed writing, review, and editing, data curation, and visualization. R.C. performed data curation, validation, and visualization. S.C. performed data curation, validation, and visualization. Z.L. performed data curation and visualization. U.A. performed data curation and visualization. J.A.H. performed funding acquisition, methodology, and supervision. S.V.V. performed methodology, project administration, resource gathering, and supervision. P.S. performed writing – review and editing, writing – original draft, conceptualization, funding acquisition, methodology, project administration, resource gathering, and supervision.

Acknowledgements

The authors thank M. Jewett and K. Zhang for help with early cell-related experimental planning. The authors also thank Z. Xiong, A.B. Merife, and A. Poudel for initial consultations on optomechanical setup, staining protocols, and print processing, respectively. Finally, the authors thank I. Gitsov for help with preliminary planning of gluing strategies. D.F. gratefully acknowledges support for his studies by the Department of Defense through the National Defense Science and Engineering Graduate (NDSEG) Fellowship Program. B.V.D. would like to acknowledge the Research Foundation – Flanders for a PhD (FWO-SB) with grant number 1SH3W24N. S.V.V. would like to thank the FWO and F.R.S.-FNRS under the Excellence of Science (EOS) program (40007548-GOJ3322N). P.S. is grateful for the financial support provided by the National Institutes of Health (NIH) R01 AR083466.

Conflicts of Interest

Z.J.G., D.F., and P.S. declare the following competing financial interest(s): A patent related to this technology is pending with Syracuse University. The other authors declare no conflicts of interest.

Data Availability Statement

All data supporting the findings of this study are available in the main text or the supporting information or can be accessed via https://github.com/psomanlab/Modular-Assembly/.

References

1. M. Kotlarz, P. Melo, A. M. Ferreira, P. Gentile, and K. Dalgarno, "Cell Seeding via Bioprinted Hydrogels Supports Cell Migration into Porous Apatite-Wollastonite Bioceramic Scaffolds for Bone Tissue Engineering," *Biomaterials Advances* 153 (2023): 213532, https://doi.org/10.1016/j.bioadv.2023.213532.

2. H. Shokrani, A. Shokrani, S. M. Sajadi, et al., "Cell-Seeded Biomaterials Scaffolds Accelerated Angiogenesis," *International Journal of Nanomedicine* 17 (2022): 1035–1068.

3. G. D. Nicodemus and S. J. Bryant, "Cell Encapsulation in Biodegradable Hydrogels for Tissue Engineering Applications," *Tissue Engineering Part B: Reviews* 14, no. 2 (2008): 149–165, https://doi.org/10.1089/ten.teb.2007.0332.

4. P. Kunwar, A. Poudel, U. Aryal, et al., "Multi-Material Gradient Printing Using Meniscus-Enabled Projection Stereolithography (MAPS)," *Advanced Materials Technologies* 10, no. 6 (2025): 2400675, https://doi.org/10.1002/admt.202400675.

5. Z. J. Geffert, Z. Xiong, J. Grutzmacher, et al., "Multipath Projection Stereolithography for Three-Dimensional Printing Microfluidic Devices," *ACS Applied Materials & Interfaces* 16, no. 50 (2024): 69807–69817, https://doi.org/10.1021/acsami.4c10547.

6. L. D. Albrecht, S. W. Sawyer, and P. Soman, "Developing 3d Scaffolds in the Field of Tissue Engineering to Treat Complex Bone Defects," *3D Printing and Additive Manufacturing* 3, no. 2 (2016): 106–112.

7. P. Soman, P. Kunwar, and Z. Xiong, "Hybrid Additive-Subtractive Laser Fabrication Platform for Shaping Hydrogels," US Patent Office, US11260596B2 (2022).

8. P. Kunwar, Z. Xiong, S. T. Mcloughlin, and P. Soman, "Oxygen-Permeable Films for Continuous Additive, Subtractive, and Hybrid Additive/Subtractive Manufacturing," *3D Printing and Additive Manufacturing* 7, no. 5 (2020): 216–221.

9. P. Kunwar, Z. Xiong, Y. Zhu, H. Li, A. Filip, and P. Soman, "Hybrid Laser Printing of 3D, Multiscale, Multimaterial Hydrogel Structures," *Advanced Optical Materials* 7, no. 21 (2019): 1900656, https://doi.org/10.1002/adom.201900656.

10. S. Zakhireh, A. Mesgari-Shadi, J. Barar, Y. Omidi, Y. Beygi-Khosrowshahi, and K. Adibkia, "Current Researches in Modular Biofabrication: Tissue Building Blocks and Bioreactors," *Korean Journal of Chemical Engineering* 41, no. 6 (2024): 1567–1585, https://doi.org/10.1007/s11814-024-00059-8.

11. D. Xing, W. Liu, J. J. Li, et al., "Engineering 3D Functional Tissue Constructs Using Self-Assembling Cell-Laden Microniches," *Acta Biomaterialia* 114 (2020): 170–182, https://doi.org/10.1016/j.actbio.2020.07.058.

12. X. Wang, Z. Wang, W. Zhai, et al., "Engineering Biological Tissues from the Bottom-Up: Recent Advances and Future Prospects," *Micromachines* 13, no. 1 (2021): 75.

13. K. J. Wolf, J. D. Weiss, S. G. M. Uzel, M. A. Skylar-Scott, and J. A. Lewis, "Biomanufacturing Human Tissues via Organ Building Blocks," *Cell Stem Cell* 29, no. 5 (2022): 667–677, https://doi.org/10.1016/j.stem.2022.04.012.

14. Z.-T. Xie, J. Zeng, S. Miyagawa, Y. Sawa, and M. Matsusaki, "3D Puzzle-Inspired Construction of Large and Complex Organ Structures for Tissue Engineering," *Materials Today Bio* 21 (2023): 100726, https://doi.org/10.1016/j.mtbio.2023.100726.

15. Z. Luo, L. Lian, T. Stocco, et al., "3D Assembly of Cryo(Bio)Printed Modular Units for Shelf-Ready Scalable Tissue Fabrication," *Advanced Functional Materials* 34, no. 4 (2024): 2309173, https://doi.org/10.1002/adfm.202309173.

16. W. Kitana, I. Apsite, and L. Ionov, "3D (Bio) Printing Combined Fiber Fabrication Methods for Tissue Engineering Applications: Possibilities and Limitations," *Advanced Functional Materials* (2025): 2500450, https://doi.org/10.1002/adfm.202500450.

17. A. Alcinesio, I. Cazimoglu, G. R. Kimmerly, V. R. Schild, R. K. Kumar, and H. Bayley, "Modular Synthetic Tissues from 3D-Printed Building Blocks," *Advanced Functional Materials* 32, no. 7 (2022): 2107773, https://doi.org/10.1002/adfm.202107773.

18. G. Yang, B. Mahadik, J. Y. Choi, et al., "Fabrication of Centimeter-Sized 3D Constructs With Patterned Endothelial Cells Through Assembly of Cell-Laden Microbeads as a Potential Bone Graft," *Acta Biomaterialia* 121 (2021): 204–213, https://doi.org/10.1016/j.actbio.2020.11.040.

19. L. Warburton, L. Lou, and B. Rubinsky, "A Modular Three-Dimensional Bioprinter for Printing Porous Scaffolds for Tissue Engineering," *Journal of Heat Transfer* 144, no. 3 (2022): 031205, https://doi.org/10.1115/1.4053198.

20. L. Suo, Y. Guo, S. Mou, et al., "Scaffold Internal Network Bioprinting for Vascularized Tissue Regeneration," *Composites Part B: Engineering* 299 (2025): 112401.

21. K. Suthiwanich and M. Hagiwara, "Localization of Multiple Hydrogels With Multicube Platform Spatially Guides 3D Tissue Morphogenesis In Vitro," *Advanced Materials Technologies* 8, no. 4 (2023): 2201660.

22. J. Zhu, Y. He, Y. Wang, and L.-H. Cai, "Voxelated Bioprinting of Modular Double-Network Bio-Ink Droplets," *Nature Communications* 15, no. 1 (2024): 5902.

23. V. Mironov, R. P. Visconti, V. Kasyanov, G. Forgacs, C. J. Drake, and R. R. Markwald, "Organ Printing: Tissue Spheroids as Building Blocks," *Biomaterials* 30, no. 12 (2009): 2164–2174.

24. K. Jakab, C. Norotte, F. Marga, K. Murphy, G. Vunjak-Novakovic, and G. Forgacs, "Tissue Engineering by Self-Assembly and Bio-Printing of Living Cells," *Biofabrication* 2, no. 2 (2010): 022001.

25. P. Zhuang, Y.-H. Chiang, M. S. Fernanda, and M. He, "Using Spheroids as Building Blocks Towards 3D Bioprinting of Tumor Microenvironment," *International Journal of Bioprinting* 7, no. 4 (2021): 444, https://doi.org/10.18063/ijb.v7i4.444.

26. Y. Zhan, W. Jiang, Z. Liu, Z. Wang, K. Guo, and J. Sun, "Utilizing Bioprinting to Engineer Spatially Organized Tissues From the Bottom-Up," *Stem Cell Research & Therapy* 15, no. 1 (2024): 101, https://doi.org/10.1186/s13287-024-03712-5.

27. D. L. Elbert, "Bottom-Up Tissue Engineering," *Current Opinion in Biotechnology* 22, no. 5 (2011): 674–680, https://doi.org/10.1016/j.copbio.2011.04.001.

28. W. Y. Wang, E. H. Jarman, D. Lin, and B. M. Baker, "Dynamic Endothelial Stalk Cell–Matrix Interactions Regulate Angiogenic Sprout Diameter," *Frontiers in Bioengineering and Biotechnology* 9 (2021): 620128.

29. W. Y. Wang, D. Lin, E. H. Jarman, W. J. Polacheck, and B. M. Baker, "Functional Angiogenesis Requires Microenvironmental Cues Balancing Endothelial Cell Migration and Proliferation," *Lab on a Chip* 20, no. 6 (2020): 1153–1166.

30. Z. M. Ruggeri, J. N. Orje, R. Habermann, A. B. Federici, and A. J. Reininger, "Activation-Independent Platelet Adhesion and Aggregation Under Elevated Shear Stress," *Blood* 108, no. 6 (2006): 1903–1910.

31. I. Roegiers, T. Gheysens, M. Minsart, et al., "Gelma as Scaffold Material for Epithelial Cells to Emulate the Small Intestinal Microenvironment," *Scientific Reports* 15, no. 1 (2025): 8214.

32. L. Maes, A. Szabó, J. V. Haevermaete, et al., "Digital Light Processing of Photo-Crosslinkable Gelatin to Create Biomimetic 3D Constructs Serving Small Intestinal Tissue Regeneration," *Biomaterials Advances* 171 (2025): 214232.

33. J. Duquesne, L. Parmentier, E. Vermeersch, et al., "Volumetric Bioprinting of the Osteoid Niche," *Biofabrication* 17, no. 2 (2025): 025002.

34. J. V. Hoorick, P. Gruber, M. Markovic, et al., "Cross-Linkable Gelatins With Superior Mechanical Properties Through Carboxylic Acid Modification: Increasing the Two-Photon Polymerization Potential," *ACS Biomacromolecules* 18 (2017): 3260–3272.

35. A. Szabó, E. D. Vlieghere, P. F. Costa, I. Geurs, K. Dewettinck, and S. V. Vlierberghe, "Increasing Hydrogel Complexity From 2D Towards 3D Towards Intestinal Tissue Engineering," *Giant* 16 (2023): 100198.

36. International Organization for Standardization. *Biological Evaluation of Medical Devices*. 10993-5:2009. Pt. 5, *Tests for in Vitro Cytotoxicity*, 2009, https://www.iso.org/standard/36406.html.

37. I. S. Kinstlinger, G. A. Calderon, M. K. Royse, A. K. Means, B. Grigoryan, and J. S. Miller, "Perfusion and Endothelialization of Engineered Tissues With Patterned Vascular Networks," *Nature Protocols* 16, no. 6 (2021): 3089–3113.

38. L. Jongpaiboonkit, W. J. King, and W. L. Murphy, "Screening for 3D Environments That Support Human Mesenchymal Stem Cell Viability Using Hydrogel Arrays," *Tissue Engineering Part A* 15, no. 2 (2009): 343–353, https://doi.org/10.1089/ten.tea.2008.0096.

39. S. W. Sawyer, S. V. Shridhar, K. Zhang, et al., "Perfusion Directed 3D Mineral Formation Within Cell-Laden Hydrogels," *Biofabrication* 10, no. 3 (2018): 035013, https://doi.org/10.1088/1758-5090/aacb42.

40. J. Almeida-Pinto, B. S. Moura, V. M. Gaspar, and J. F. Mano, "Advances in Cell-Rich Inks for Biofabricating Living Architectures," *Advanced Materials* 36, no. 27 (2024): 2313776.

41. M. C. Decarli, A. Seijas-Gamardo, F. L. C. Morgan, et al., "Bioprinting of Stem Cell Spheroids Followed by Post-Printing Chondrogenic Differentiation for Cartilage Tissue Engineering," *Advanced Healthcare Materials* 12, no. 19 (2023): 2203021.

42. M. Kappes, B. Friedrich, F. Pfister, et al., "Superparamagnetic Iron Oxide Nanoparticles for Targeted Cell Seeding: Magnetic Patterning and Magnetic 3D Cell Culture," *Advanced Functional Materials* 32, no. 50 (2022): 2203672.

43. B. Ayan, N. Celik, Z. Zhang, et al., "Aspiration-Assisted Freeform Bioprinting of Pre-Fabricated Tissue Spheroids in a Yield-Stress Gel," *Communications Physics* 3, no. 1 (2020): 183, https://doi.org/10.1038/s42005-020-00449-4.

44. N. I. Moldovan, N. Hibino, and K. Nakayama, "Principles of the Kenzan Method for Robotic Cell Spheroid-Based Three-Dimensional Bioprinting," *Tissue Engineering Part B, Reviews* 23, no. 3 (2017): 237–244.

45. N. Zeinstra, A. L. Frey, Z. Xie, et al., "Stacking Thick Perfusable Human Microvascular Grafts Enables Dense Vascularity and Rapid Integration into Infarcted Rat Hearts," *Biomaterials* 301 (2023): 122250.

46. J. Takahashi, H. Y. Sugihara, S. Kato, et al., "Controlled Aggregative Assembly to Form Self-Organizing Macroscopic Human Intestine From Induced Pluripotent Stem Cells," *Cell Reports Methods* 4, no. 12 (2024): 100930.

47. J. G. Roth, L. G. Brunel, M. S. Huang, et al., "Spatially Controlled Construction of Assembloids Using Bioprinting," *Nature Communications* 14, no. 1 (2023): 4346.

48. J. Kim, K. Imaizumi, O. Jurjuț, et al., "Human Assembloid Model of the Ascending Neural Sensory Pathway," *Nature* 642 (2025): 143–153.

49. M. A. Skylar-Scott, S. G. M. Uzel, L. L. Nam, et al., "Biomanufacturing of Organ-Specific Tissues With High Cellular Density and Embedded Vascular Channels," *Science Advances* 5, no. 9 (2019): aaw2459, https://doi.org/10.1126/sciadv.aaw2459.

50. A. C. Daly and D. J. Kelly, "Biofabrication of Spatially Organised Tissues by Directing the Growth of Cellular Spheroids Within 3D Printed Polymeric Microchambers," *Biomaterials* 197 (2019): 194–206.

51. M. H. Kim, Y. P. Singh, N. Celik, et al., "High-Throughput Bioprinting of Spheroids for Scalable Tissue Fabrication," *Nature Communications* 15, no. 1 (2024): 10083, https://doi.org/10.1038/s41467-024-54504-7.

52. D. G. Hwang, H. Choi, U. Yong, et al., "Bioprinting-Assisted Tissue Assembly for Structural and Functional Modulation of Engineered Heart Tissue Mimicking Left Ventricular Myocardial Fiber Orientation," *Advanced Materials* 36, no. 34 (2024): 2400364.

53. M. Lovett, K. Lee, A. Edwards, and D. L. Kaplan, "Vascularization Strategies for Tissue Engineering," *Tissue Engineering Part B: Reviews* 15, no. 3 (2009): 353–370, https://doi.org/10.1089/ten.teb.2009.0085.

54. A. M. Blakely, K. L. Manning, A. Tripathi, and J. R. Morgan, "Bio-Pick, Place, and Perfuse: A New Instrument for Three-Dimensional Tissue Engineering," *Tissue Engineering Part C, Methods* 21, no. 7 (2015): 737–746.

55. R. Subbiah, C. Hipfinger, A. Tahayeri, et al., "3D Printing of Microgel-Loaded Modular Microcages as Instructive Scaffolds for Tissue Engineering," *Advanced Materials* 32, no. 36 (2020): 2001736.

56. Q. Gao, Z. Liu, Z. Lin, et al., "3D Bioprinting of Vessel-Like Structures With Multilevel Fluidic Channels," *ACS Biomaterials Science & Engineering* 3, no. 3 (2017): 399–408, https://doi.org/10.1021/acsbiomaterials.6b00643.

57. B. Li, Z. Wang, C. Huang, et al., "A Comprehensive Review on the Printing Efficiency, Precision, and Cell Viability in 3D Bioprinting," *Medical Engineering & Physics* 145, no. 1 (2025): 104448, https://doi.org/10.1016/j.medengphy.2025.104448.

58. K. Dubbin, A. Tabet, and S. C. Heilshorn, "Quantitative Criteria to Benchmark New and Existing Bio-Inks for Cell Compatibility," *Biofabrication* 9, 4 (2017): 044102, https://doi.org/10.1088/1758-5090/aa869f.

59. S. You, Y. Xiang, H. H. Hwang, et al., "High Cell Density and High-resolution 3D Bioprinting for Fabricating Vascularized Tissues," *Science Advances* 9, no. 8 (2023), https://doi.org/10.1126/sciadv.ade7923.

60. N. He, X. Wang, L. Shi, et al., "Photoinhibiting Via Simultaneous Photoabsorption and Free-Radical Reaction for High-Fidelity Light-Based Bioprinting," *Nature Communications* 14, no. 1 (2023), https://doi.org/10.1038/s41467-023-38838-2.

61. A. Cosola, A. Chiappone, and M. Sangermano, "Changing the Surface Properties With a "Click": Functionalization of Dlp-Printed Structures Exploiting Residual Acrylate Functions," *Molecular Systems Design & Engineering* 7, no. 9 (2022): 1093–1101.

62. M. Markovic, J. Van Hoorick, K. Hölzl, et al., "Hybrid Tissue Engineering Scaffolds by Combination of Three-Dimensional Printing and Cell Photoencapsulation," *Journal of Nanotechnology in Engineering and Medicine* 6, no. 2 (2015): 021001, https://doi.org/10.1115/1.4031466.

Supporting Information

Additional supporting information can be found online in the Supporting Information section.

Supporting File: adfm75239-sup-0001-SuppMat.docx.